

Mercury Vapor Air-Surface Exchange Measured by Collocated

2 Micrometeorological and Enclosure Methods – Part I: Data Comparability and
Method Characteristics

4 W. Zhu^{1,2}, J. Sommar^{1,*}, C.-J. Lin^{1,3,4}, X. Feng^{1,*}

¹ State Key Laboratory of Environmental Geochemistry, Institute of Geochemistry, Chinese Academy of
6 Sciences, Guiyang 550002, China

² University of Chinese Academy of Sciences, Beijing 100049, China

8 ³ Department of Civil Engineering, Lamar University, Beaumont, TX 77710, United States

⁴ College of Environment and Energy, South China University of Technology, Guangzhou 510006, China

10

12 *Correspondence to: X. Feng (fengxinbin@vip.skleg.cn) and J. Sommar (jonas@vip.skleg.cn)

X. Feng, phone: +86 851 5891356, fax: +86 851 5891609; e-mail: fengxinbin@vip.skleg.cn

14 J. Sommar, phone: +86 158 85096925, fax: +86 851 5891609; e-mail: jonas@vip.skleg.cn

16

ABSTRACT

18 Reliable quantification of air-biosphere exchange flux of elemental mercury vapor (Hg^0) is crucial for
understanding global biogeochemical cycle of mercury. However, there has not been a standard analytical
20 protocol for flux quantification, and little attention has been devoted to characterize the temporal
variability and comparability of fluxes measured by different methods. In this study, we deployed a
22 collocated set of micro-meteorological (MM) and [dynamic flux chambers \(DFCs\)](#) measurement systems to
quantify Hg^0 flux over bare soil and low standing crop in an agricultural field. The techniques include
24 relaxed eddy accumulation (REA), modified Bowen-ratio (MBR), aerodynamic gradient (AGM) as well as
dynamic flux chambers of traditional (TDFC) and novel (NDFC) designs. The five systems and their
26 measured fluxes were cross-examined with respect to magnitude, temporal trend and [correlation with](#)
environmental variables.

28 Fluxes measured by the MM and DFC methods showed distinct temporal trends. The former
exhibited a highly dynamic temporal variability while the latter had much gradual temporal features. The
30 diurnal characteristics reflected the difference in the fundamental processes driving the measurements. The
correlations between NDFC and TDFC fluxes and between MBR and AGM fluxes were significant ($R >$
32 0.8 , $p < 0.05$), but the correlation between DFC and MM fluxes were from weak to moderate ($R = 0.1-0.5$).
Statistical analysis indicated that the median of turbulent fluxes estimated by the three independent
34 MM-techniques were not significantly different. Cumulative flux measured by TDFC is considerably lower
(42% of AGM and 31% of MBR fluxes) while those measured by NDFC, AGM and MBR were similar (<
36 10% difference). [This suggests that incorporating an atmospheric turbulence property such as friction](#)
[velocity for correcting the DFC-measured flux effectively bridged the gap between the \$\text{Hg}^0\$ fluxes](#)
38 [measured by enclosure and MM techniques](#). Cumulated flux measured by REA was ~60% higher than the
gradient-based fluxes. Environmental factors have different degrees of impacts on the fluxes observed by
40 different techniques, possibly caused by the underlying assumptions specific to each individual method.
Recommendations regarding the application of flux quantification methods were made based on the data
42 obtained in this study.

44

1. Introduction

46 Mercury (Hg) is a ubiquitously distributed neurotoxin in the environment (Lindqvist et al., 1991). The bulk
of atmospheric Hg is made up of gaseous elemental Hg (Hg^0 , >95% of the total mass) with minor
48 contribution from the analytically defined fractions of gaseous oxidized Hg (GOM) and particulate
bounded Hg (PBM) (Gustin, 2011). Being chemically inactive and partitioning less favorably into aqueous
50 phase, Hg^0 is prone to undergo hemispherical-scale tropospheric transport (Durnford et al., 2010). Hg^0 is
subject to bi-directional exchange between atmosphere and natural surfaces through complex and yet not
52 well understood processes (Bash, 2010;Gustin and Jaffe, 2010). Recent estimation indicates that annual
natural emission accounts for two-thirds of global release of atmospheric Hg (Pirrone et al., 2010).
54 However, current estimates of natural exchange quantity remain highly uncertain due to the limitations in
accuracy and representativeness of measurement techniques (Gustin and Jaffe, 2010;Pirrone et al., 2010).

56 There exist multiple experimental approaches to gauge Hg^0 air-surface exchange, which can be
grouped into enclosure and micrometeorological (MM) methods (Sommar et al., 2013a). Dynamic flux
58 chambers (DFCs) representing the smallest scale as the areas covered are typically in the order of 0.1 m^2 ,
are the most extensively applied method for quantifying Hg^0 evasion from and deposition to soil (Poissant
60 and Casimir, 1998;Stamenkovic and Gustin, 2007;Xiao et al., 1991;Carpi and Lindberg, 1998). For
measuring Hg^0 fluxes on larger landscape scales, MM techniques represent an attractive alternative to DFCs.
62 They allow spatially averaged measurements over a large area without disturbing ambient environmental
conditions. For trace gases such as CO_2 , CH_4 , O_3 , NH_3 , HNO_3 , and selected VOCs, eddy covariance (EC)
64 is the preferred MM technique for quantifying air-landscape gas exchange (Aubinet et al., 2012; Farmer et
al., 2006; Park et al., 2013;Whitehead et al., 2008). However, due to the lack of a sufficiently fast and
66 sensitive sensor for the ultra-trace levels of Hg^0 in air, true EC measurement of background Hg^0 flux has

not yet been [accomplished](#). MM techniques applied in Hg^0 flux (also called turbulent flux) quantification including the relaxed eddy accumulation method (REA, also known as conditional sampling, CS) ([Bash and Miller, 2008](#); [Cobos and Baker, 2002](#); [Olofsson et al., 2005](#); [Sommar et al., 2013b](#)), the aerodynamic gradient methods (AGM) ([Baya and Van Heyst, 2010](#); [Cobbett and Van Heyst, 2007](#); [Converse et al., 2010](#); [Edwards et al., 2005](#); [Fritsche et al., 2008a](#); [Fritsche et al., 2008b](#); [Marsik et al., 2005](#)), and the modified Bowen ratio method (MBR) ([Converse et al., 2010](#); [Fritsche et al., 2008a](#); [Fritsche et al., 2008b](#); [Lindberg et al., 1995](#); [Poissant et al., 2004](#)). MM methods estimate turbulent transport with the assumptions of fetch homogeneity and the measurements are made within the constant flux layer ([Wesely and Hicks, 2000](#)). For example, REA-derived flux relying on accurate measurement of the concentration difference between upward and downward moving air parcels while gradient-derived flux is estimated from the vertical concentration gradient and the associated turbulent exchange parameters. For the traditional DFC (TDFC) methods, flux is derived from a steady-state mass balance over the chamber. More recently, we have designed and deployed a DFC of novel design (NDFC) based on surface wind shear condition (friction velocity) rather than on artificial fixed flow to account for natural shear conditions ([Lin et al., 2012](#)).

Limited efforts have been devoted to Hg^0 flux measurement comparison. In the Nevada STORMS campaign ([4 days duration](#)), TDFCs and MM gradient methods were deployed to measure Hg^0 flux over a heterogeneously Hg-enriched fetch. The TDFC- and MM-derived fluxes differed by one order of magnitude ([Gustin et al., 1999](#); [Gustin and Lindberg, 2000](#); [Poissant et al., 1999](#); [Wallschläger et al., 1999](#)). Subsequent investigations have suggested that TDFCs of different sizes, shapes and operation flow rates yield different fluxes ([Eckley et al., 2010](#); [Lin et al., 2012](#); [Zhang et al., 2002](#); [Wallschläger et al., 1999](#)). Gradient methods were deployed to measure seasonal Hg^0 fluxes over grasslands in the Alps ([Fritsche et](#)

al., 2008b) and over a meadow in the Appalachians (Converse et al., 2010), the observed flux means varied
90 by up to one order of magnitude. Collocated flux measurement using both MM and DFCs techniques for
method evaluation and data synthesis remains scarce (Gustin, 2011). This limits a thorough comparison of
92 flux data obtained by different techniques.

Measured fluxes are estimates of unknown quantities of air-surface exchange under field conditions
94 and a reference technique for validating the estimates does not exist. Each available technique has its
specific advantages and drawbacks and its applicability to obtain representative fluxes is limited under
96 particular atmospheric conditions and site characteristics. It is therefore essential to compare and review
uncertainties of the major techniques deployed for measuring air-ecosystem Hg^0 exchange. The objective
98 of this study is to investigate the method characteristics, data comparability and measurement uncertainty
of Hg^0 exchange fluxes as measured by five collocated MM and DFC methods including REA, MBR,
100 AGM, TDFC, and NDFC. We improved a number of measurement platforms (Lin et al., 2012; Sommar et
al., 2013b) and performed two intensive field campaigns over both bare and vegetated landscapes. The
102 results of this integrated assessment are presented in part by two companion papers. In Part I, we evaluate
the technical merits of the examined flux quantification methods, assess the flux variability and data
104 comparability, and address the method applicability under a given set of environmental conditions. In Part
II, we quantify the bias and uncertainty of the examined flux measurement methods.

106

2. Material and methods

2.1. Flux measurement methods

2.1.1 Dynamic flux chamber techniques

110 In this study, chambers of traditional and the new design described in Lin et al. (2012) were

inter-compared. The hemi-cylindrical TDFC made of quartz with an open bottom area of 0.06 m² has been
 112 used extensively in our group and elsewhere (Feng et al., 2005;Fu et al., 2008;Fu et al., 2012;Fu et al.,
 2010;Li et al., 2010;Wang et al., 2005;Wang et al., 2007;Zhu et al., 2013a). The NDFC was fabricated of
 114 thin polycarbonate sections and enclosed a soil surface of 0.09 m² (for details, see Lin et al., 2012). The
 NDFC internal flow condition was precisely controlled to relate to the applied flushing flow rate to the
 116 atmospheric boundary shear condition (therefore wind shear condition) and the calculated flux was
 re-scaled to boundary shear condition (Equation 2 below). Both DFCs were operated at a relatively high
 118 flushing flow rate of 15 L min⁻¹, corresponding to turn-over times (TOTs) of 0.32 min and 0.47 min for
 TDFC and NDFC, respectively. The flux from TDFC and NDFC were calculated following Eq. (1) and (2),
 120 respectively (Xiao et al., 1991; Lin et al., 2012):

$$F_{Hg^0}^{TDFC} = \frac{Q(C_o - C_i)}{A} \quad (1)$$

$$F_{Hg^0}^{NDFC} = \frac{Q(\Delta C)}{A} \frac{k_{mass(a)}}{k_{mass(m)}} = \frac{Q(C_o - C_i)}{A} \frac{\left(4.86 + \frac{0.03(h/l)[hu_*/(6kz_0)](D_H/D)}{1 + 0.016\{(h/l)[hu_*/(6kz_0)](D_H/D)\}^{2/3}} \right)}{\left(4.86 + \frac{0.03(h/l)(Q/A_c)(D_H/D)}{1 + 0.016[(h/l)(Q/A_c)(D_H/D)]^{2/3}} \right)} \quad (2)$$

where $F_{Hg^0}^{TDFC}$ is Hg⁰ flux measured from TDFC method, $F_{Hg^0}^{NDFC}$ is Hg⁰ flux from NDFC method, Q
 124 is applied flow rate (0.9 m³ h⁻¹), A is footprint (0.06 m² for TDFC, 0.09 m² for NDFC), C_o and C_i
 are the DFC outlet and inlet air Hg⁰ concentration, $k_{mass(a)}$ and $k_{mass(m)}$ are the overall mass transfer
 126 coefficient (m s⁻¹) in the near-surface boundary layer and in the internal layer within NDFC, respectively.
 A_c is the NDFC flow cross-sectional area (0.009 m²), l is the distance measured from the starting point
 128 of the measurement zone (0.15 m), h is the height of NDFC (0.03 m), u_* is the atmospheric boundary
 layer friction velocity, and z_0 is surface roughness height (m). D_H and D are the NDFC hydraulic
 130 radius (0.0545 m) and diffusivity of Hg⁰ (1.194 × 10⁻⁵ m² s⁻¹), respectively.

132 **2.1.2 Micrometeorological techniques**

Relaxed eddy accumulation (REA) method

134 A REA system of whole-air type was deployed with the design and operation parameters described
elsewhere (Sommar et al., 2013b;Zhu et al., 2013b). The REA apparatus constitutes of open path EC
136 (OPEC) and conditional gas sampling system. The OPEC part included a 3D fast-response anemometer, an
open path CO₂/H₂O analyzer, and a micro-logger with processing and control capabilities. MM data
138 collected at 10 Hz is acquired and processed by the latter, which also control the execution of conditional
sampling valves from its 12 V terminal following the implemented dynamic wind dead-band algorithm to
140 accurately isolate up- and down-drafts present in sampled turbulent air parcels. Turbulent REA flux was
computed according to:

$$142 \quad F_{Hg^0}^{REA} = \beta_s \sigma_w \underbrace{\left(\overline{C^\uparrow} - \overline{C^\downarrow} \right)}_{\Delta C_{REA}} = \beta_s \sigma_w \left\{ \sum_i \frac{m_i^\uparrow}{t_i \cdot Q_i^\uparrow \cdot \alpha_i^\uparrow} - \sum_i \frac{m_i^\downarrow}{t_i \cdot Q_i^\downarrow \cdot \alpha_i^\downarrow} \right\} \quad (3)$$

where σ_w (m s⁻¹) is the standard deviation of vertical wind speed (m s⁻¹) and $C^{\uparrow/\downarrow}$ is the concentration
144 of Hg⁰ (at standard temperature and pressure) for the up- and down-moving eddies corrected for dilution of
zero air injection, respectively (ng m⁻³). The operational form of Eq. 3 is given on the right-hand side, in
146 which, for sample i , $m_i^{\uparrow/\downarrow}$ is the mass of Hg⁰ derived for the up- or down-draft channels (pg), t_i is the
total duration (min), $Q_i^{\uparrow/\downarrow}$ is the continuous flow rate through the up- or down-draft channels (L dry air
148 min⁻¹), and $\alpha_i^{\uparrow/\downarrow}$ is the fraction of time the up- or down-draft conditional sample valves are activated.
 β_s is a dimensionless relaxation coefficient (calculated from scalar s) which for each averaging period
150 (20 min) was calculated on-line from suitable scalar s those fluxes ($F_s^{EC} = \overline{\rho_d \cdot w' \chi'_s}$) can be measured by
the OPEC system (in addition to CO₂ flux, buoyancy flux $C_p \cdot \overline{w' T'_s}$ and for latent heat flux $\lambda \cdot \overline{w' q'}$,

152 symbol definitions see appendix in [Sommar et al., \(2013b\)](#)) as well as by REA according to:

$$\beta_s = \overline{w' \chi_s'} / \left[\sigma_w \left(\overline{\chi_s^\uparrow} - \overline{\chi_s^\downarrow} \right) \right] \quad (4)$$

154 where $\chi_s^{\uparrow/\downarrow}$ is the mixing ratio of the specific scalar quantity for the up- and downdraft (kg kg^{-1}).

Aerodynamic gradient micrometeorological (AGM) method

156 The AGM method is based on an analogy application of Fick's first law stating that turbulent
bi-directional flux of a scalar from surface (F_s^{AGM}) is proportional to its local vertical concentration
158 gradient ($\partial C / \partial z$) and eddy diffusivity of sensible heat (K_H), which is a function of friction velocity (u_*)

and the dimensionless stability parameter $\zeta_m = (z_m - d) / L$ (z_m is the sampling height above ground, d
160 is the zero plane displacement height and L is the Monin-Obukhov length ([Monin and Obukhov, 1954](#)).

Assuming measurements are made within a vertical layer of constant flux that forms over homogeneous
162 terrain, after integration between two heights, the flux can be expressed as:

$$F_{Hg^0}^{AGM} = -K_H(u_*, \zeta) \frac{\partial C}{\partial z} = - \frac{\kappa u_*}{\underbrace{\ln \left(\frac{z_2 - d}{z_1 - d} \right) - \psi_H(\zeta_2) + \psi_H(\zeta_1)}_{v_{tr}}} \cdot \underbrace{(C_{z_2} - C_{z_1})}_{\Delta C} \quad (5)$$

164 where κ is von Kármán constant (~ 0.41), u_* is the friction velocity (m s^{-1}), v_{tr} term is the transfer
velocity (m s^{-1}), z_2 and z_1 are the heights of the upper and lower sampling inlet (m), ψ_H is the

166 integrated universal function for sensible heat to correct for deviations from the ideal logarithmic profile.

ψ_H is parameterized as a function of ζ_m (ζ_1 and ζ_2 represents the parameter at z_2 and z_1
168 respectively), and furthermore C_{z_2} and C_{z_1} are the Hg^0 concentration (ng m^{-3}) at z_2 and z_1 ,
respectively.

170 Modified Bowen-ratio (MBR) method

MBR method assumes that the flux of a trace gas can be related to that of a surrogate scalar
172 determined from OPEC measurements (e.g., sensible and latent heat, CO_2 flux, and H_2O flux) ([Converse et](#)

al., 2010; Lindberg et al., 1995). In this study, temperature was used as the proxy scalar, which was
174 monitored at the heights coinciding with measurement of Hg⁰ concentration. The Hg⁰ flux is calculated
following Walker et al. (2006):

$$176 \quad F_{\text{Hg}^0}^{\text{MBR}} = \overline{w'T'} \cdot \frac{C(z_2) - C(z_1)}{T(z_2) - T(z_1)} = \overline{w'T'} \cdot \frac{\Delta C}{\Delta T} \quad (6)$$

where $F_{\text{Hg}^0}^{\text{MBR}}$ is the Hg⁰ flux (ng m⁻² h⁻¹) measured with MBR method, $\overline{w'T'}$ is kinematic heat flux (K
178 m s⁻¹) measured by EC, while ΔC and ΔT are the vertical gradients of Hg⁰ concentration (ng m⁻³) and air
temperature (K), respectively. The ratio $\overline{w'T'}/\Delta T$ is known as eddy diffusivity for heat.

180

2.2 Site description and sampling

182 The flux measurement experiments were conducted at Yucheng Comprehensive Experimental Station,
Chinese Academy of Sciences (36°57'N, 116°36'E), which is a semi-rural agricultural station located in the
184 North China Plain approximately 50 km from Jinan, Shandong Province. Within a radius of ~5 km the
planting system is winter wheat (*Triticum aestivum* Linn., November - May) or summer maize (*Zea mays*,
186 June - October) for a rotation in a year. The surface soil texture in this area is silty loam consists of 12%
sand, 22% clay and 66% silt with moderate salinity and alkalinity (pH = 8.6) (Hou et al., 2012). The
188 agricultural fields adjacent to the sampling site are relatively flat (level differences < 1.5 m within 1 km)
and the total Hg content in surface soil is spatial homogeneously distributed (45 ± 3.9 μg kg⁻¹, n=27) (Zhu et
190 al., 2014b). Two intensive field campaigns were performed: one in late autumn 2012 (IC #1, November 4th
- 24th, DOY (day of year) 309 - 329) and the other in spring 2013 (IC #2, April 16th -to 25th, DOY 106
192 -115). IC #1 was carried out over the ploughed bare soil surface using AGM, MBR, TDFC, and NDFC. IC
#2 was carried out over wheat canopy (average height ~0.36 m, leaf area index of 3.4) using REA, AGM,
194 and MBR. Given the tight row spacing of the grain field, the deployment of DFCs was not permissible

during IC#2.

196 2.3 Instrumentation

198 A 6.5 m MM flux tower was installed at the same location for both campaigns (Fig. 1). The instrumentation system constitutes of the tower based MM systems and ground based DFCs. The OPEC system consisted of a Campbell CSAT-3 sonic anemometer-thermometer, Licor LI-COR 7500A open-path CO₂/H₂O analyzer and HMP155A humidity-temperature sensors, a standard instrumentation combination used in long-term ecosystem instrumentation networks (Mauder et al., 2013). REA sampling inlet was positioned at 2.96 m above ground. By using a set of 2/3-way automated magnetic switching unit (Tekran® 1110) coupled with an automated Tekran® 2537B Hg⁰ vapor analyzer operated at a flow rate of 0.75 L min⁻¹, up- and down-draft conditional samples was sequentially routed into the analyzer at 10-min intervals (two 5-min samples). For gradient measurements, the temperature and relative humidity sensor (HMP155A, Vaisala Oy, Finland) housed in radiation shields and corresponding Hg⁰ intake was assembled at two heights of 2.96 m and 0.76 m. The two-level Hg⁰ vertical gradient profiling system consisted of two separate inlet lines (PFA Teflon), each with an inlet filter (0.2-µm PFA Teflon), were routed to another sampling manifold (Model 1110). Another Hg⁰ gas analyzer (Model 2537B) is connected to the outlet of the manifold and the profile inlets are opened one at a time synchronized with 2537B's sampling cycles. The manifold was configured to allow the inlet not in use to be continually flushed by a bypass pump. Both the pump and 2537B are operated at a flow rate of 1.0 L min⁻¹. An estimate of the vertical Hg⁰ concentration gradient was derived every 20 min from measurements of the two heights sequentially, 5 min integrated samples.

The TDFC and NDFC were operated in tandem using one 2537B analyzer (sampling flow rate 1.0 L min⁻¹). A 4-port automated magnetic dual switching unit (Tekran® 1115) was utilized to sequentially

sample the two DFCs inlet and outlet twice at 2.5-min intervals in the sequential order: inlet of TDFC,
218 outlet of TDFC, inlet of NDFC, and outlet of NDFC, whereby retrieving 2.5 L samples for Hg⁰ analysis.
20-min Hg⁰ flux was calculated using Eq. (1) and (2) for TDFC and NDFC. Prior to sampling, the internal clocks of
220 all instrumentation were synchronized (UTC +8h) and therefore the reported fluxes resembled identical 20-min
integration periods.

222

2.4 Quality assurance/control (QA/QC), data evaluation and EC flux corrections

224 The three Tekran[®] 2537B analyzers (Fig. 1) were operated and maintained following the standard
operation procedures of NADP, 2011. The analyzers were regularly calibrated in the laboratory by manual
226 injections of known amount of Hg⁰. The yielded recovery was 98%-101%. In the field, instruments were
calibrated every 48 h using the internal Hg⁰ permeation source. A soda-lime trap and a 0.2- μ m Teflon
228 membrane filter were located upstream the inlet of all analyzers. The analyzers are sensitive to insufficient
power and were therefore always supplied with grid power passing a 10-kW voltage stabilizer to ensure
230 proper operation in the field. All the tubing and system valve blanks were checked before and after the
campaigns by flushing with zero air obtained from a zero-air generator (Tekran[®] 1100). Before the field
232 measurement, the accuracy of two HMP 155A sensors was evaluated after periods of side-by-side
measurements. The two DFCs were cleaned by 10% HNO₃ and Milli-Q water prior to field deployment.
234 Chamber blanks performed at the field site were consistently low for both DFCs (TDFC: 0.2 ± 0.1 ng m⁻²
h⁻¹, n=19; NDFC: 0.3 ± 0.2 ng m⁻² h⁻¹, n=32) and not subtracted upon calculation of fluxes.

236 The REA-system enabled a mode during which air is sampled synchronously with both conditional inlets.
This reference mode provides an automated QC-measure to regularly check for gas sampling path bias, while the
238 gradient-based MM techniques require manual testing by collocating gas sampling inlets and sensors. Such

side-by-side tests were performed before or after a campaign. Post processing of collected 10 Hz EC raw data
240 was performed for each of the 20-min flux averaging periods using Eddypro™ 5.0 flux analysis software
package (LI-COR Biosciences Inc.). A series of standard data corrections were implemented following
242 (Sommar et al., 2013b) including the Webb-Pearman-Leuning (WPL) correction. Moreover, tests were
applied on 20-min fast time (10 Hz) series raw data to qualitatively assess turbulence for the assumptions
244 required of applying MM methods (steady-state conditions and the fulfillment of similarity conditions).
The basic flag system of Mauder and Foken (2004) was utilized to indicate limitation in turbulence mixing,
246 quality indices of 0, 1, and 2 denoted high, moderate and low quality.

248 **2.5 Meteorological data**

Supporting meteorological data (sampled at 1 Hz and stored as 20 min averages), including relative
250 humidity (RH, %), canopy leaf wetness (%), air temperature (°C), event-based rainfall (mm), wind speed
(m s^{-1}), wind direction (°), solar radiation (W m^{-2}), soil temperature (°C), and soil moisture ($\text{m}^{-3} \text{ m}^{-3}$) were
252 acquired using a portable weather station (HOBO U30, Onset Corp., USA) equipped with a suite of
sensors positioned on a mast of 3 m height.

254

3. Results and Discussion

256 **3.1 Meteorological conditions**

Meteorological observations and ambient Hg^0 concentration during the two campaigns are presented
258 in Fig. 2 and summarized in Table 1. The weather was predominantly sunny and temperate (-3.5 to 15.1°C
during IC #1 and 0.8 to 17.4°C during IC #2). A rain shower yielding 3.4-mm precipitation occurred
260 during IC #1. No precipitation was recorded during IC #2 (Fig. 2 upper panel). Leaf wetness and RH

displayed clear diurnal variation (RH dropped to 40% and leaf wetness to 0% during daytime) except
262 during the precipitation event when both were near saturation. Due to the high RH and sometimes sub-zero
temperature at night, the ground and wheat possessed intermittently a light frost cover in early morning
264 time. The wind speed was relatively high during daytime and turned moderate/calm at night. The wind
direction was more variable from south to northeast with an average wind speed at 1.52 m s⁻¹ (daytime
266 mean: 1.98 m s⁻¹, nighttime mean: 1.05 m s⁻¹) in IC #1, and changed to southwest and northeast with a
mean of 2.69 m s⁻¹ (daytime mean: 3.34 m s⁻¹, nighttime mean: 1.97 m s⁻¹) in IC #2. The wind directions in
268 IC #2 were more consistent than in IC #1, ~60% of 20-min wind observations were of southwesterly
directions (Fig. 3A & Fig. 3C). The integral turbulence characteristics are indicated by σ_w/u_* (Panofsky
270 and Dutton, 1984). For neutral stratification, this ratio is approximately constant at 1.13 - 1.35 (Nemitz et
al., 2009). The median σ_w/u_* was 1.28 and 1.24 during IC #1 and IC #2. However, the variability
272 introduced by diabatic condition is comparatively more pronounced during IC #1. Hg⁰ observations at the
sampling site showed a wide range of 1.20 to 8.17 ng m⁻³ (medians 3.12 ng m⁻³ and 3.50 ng m⁻³ during IC
274 #1 and #2, respectively). The medians were elevated compared to the hemispheric background (1.5 - 1.7 ng
m⁻³), but nevertheless appeared representative of a semi-rural area of North China plain (~3.2 ng m⁻³,
276 Zhang et al., 2013). The angular distribution of Hg⁰ observations (Fig. 3B & Fig. 3D) indicated a weak Hg⁰
concentration dependence on wind direction during IC #1 but a more manifest dependence appeared
278 during IC #2, with elevated concentrations associated with southerly and south-westerly winds (4.04 - 4.88
ng m⁻³, 45% - 130% higher than those associated with easterlies, 2.12 - 2.79 ng m⁻³).

280

3.2 Hg⁰ fluxes observed by the DFC techniques

282 3.2.1 Characteristics of DFCs Hg⁰ fluxes

Descriptive statistics of the DFC Hg^0 flux observations are presented in Table 1. In a comparison,
284 NDFC-derived Hg^0 fluxes spanned over a broader range and exhibited a higher mean. Fig. 4a displays the
time series of Hg^0 fluxes gauged by the two DFC methods. Both series showed similar diurnal features
286 with daytime evasion (maximum occurred at midday) and a shallow minimum of bi-directional exchange
during nighttime. The pattern is consistent with observations made over background soils worldwide
288 (Gustin et al., 2011 and the references therein).

The median \pm MAD (median absolute deviation) of Hg^0 flux were -0.9 ± 3.2 and $-1.7 \pm 4.3 \text{ ng m}^{-2} \text{ h}^{-1}$
290 for TDFC and NDFC, respectively. Probability plots of both DFC datasets showed positive kurtosis (3.0
and 4.1) and skewness (1.6 and 2.1) (Fig. 5) as a consequence of stronger emission and increased friction
292 velocity at daytime. The substantial fraction of NDFC data points elevated in magnitude outlying
 $1.5 \cdot IQR$ (interquartile range) bound is associated to periods of high wind speed (i.e. showing the
294 dependence of friction velocity in Eq. 2). Moreover, as indicated in Fig. 5, the shortest half (50%) of the
chamber flux data is positioned more towards dry deposition for the novel compared to the traditional
296 chamber technique. Nevertheless, the intrinsic divergence of the microenvironment inside enclosures in
relation to that of near-surface air layer tends to promote efflux.

298

3.2.2 Comparison of Hg^0 fluxes obtained from DFCs measurement

300 In the Nevada STORMS campaign, seven flow-through enclosures (DFCs) with different operational
parameters and designs were located in an arid area with naturally Hg-enriched substrate. The observed
302 DFC Hg^0 fluxes showed similar diurnal profiles but diverged in magnitude by an order of magnitude
(Gustin et al., 1999; Wallschlager et al., 1999; Gustin and Lindberg, 2000). The observed difference was
304 partially attributed to the substrate heterogeneity with respect to Hg content. In this study, the surface soil

Hg content within the methodological footprint range is at large homogeneous and therefore not pose an
306 interfering factor.

Eckley et al. (2010) examined experimentally a series of operational and instrumental factors that may
308 influence DFC-derived flux. The DFC flushing flow rate was identified to have substantial positive
influence. In the present study, turn over time (TOT) of TDFC is 50% smaller than that of the NDFC.
310 Moreover, the footprint of the traditional type is about two-thirds of the NDFC footprint and therefore a
higher fluxes is expected using the NDFC method (Eckley et al., 2010; Lin et al., 2012). Fig. 6 shows a
312 scatter plot of the fluxes measured by the NDFC and TDFC approach before and after turbulence
correction. The data were significantly positive correlated ($R = 0.93$, $R = 0.95$ between TDFC and NDFC
314 fluxes calculated with Eq.2, Eq.1, respectively; $p < 0.01$). Quantitatively, direct measured flux was
consistent for the two chambers (slope 1.01). After accounting for the atmospheric boundary shear
316 condition by Eq. 2, the well-developed turbulence (higher friction velocity, Fig. 2) during daytime caused
the NDFC-inferred Hg^0 flux to be approximately 2.5 times higher than the TDFC flux. Given that fluxes
318 derived from a DFC of conventional type do not allow for re-scaling to represent natural surface shear
stress conditions, TDFCs are prone to underestimate the soil Hg emission, particularly when operated at
320 low air exchange rates. The ability to incorporate an atmospheric turbulence property such as friction
velocity makes the NDFC method a more favorable approach for estimating Hg^0 gas exchange over soils
322 compared to the TDFC method.

3.3 Hg^0 fluxes inferred from MM methods

3.3.1 *Characteristics of Turbulent Hg^0 fluxes observed by micrometeorological methods*

326 Fig. 4 A&B show the time-series of normalized vertical Hg^0 concentration gradient ($ng\ m^{-4}$) and Hg^0

flux ($\text{ng m}^{-2} \text{ h}^{-1}$) derived from the turbulent diffusion methods (MBR and AGM). Hg^0 concentration
328 gradients were observed in the similar ranges of -0.49 to 0.33 and -0.48 to 0.25 ng m^{-4} in both campaigns
(Table 1 and Fig. 4), though the more occasionally shifting conditions of weak and developed turbulence in
330 IC #1 tend towards promoting a higher scale of diurnal gradient variability (IC #1 vs IC #2 standard
deviation: 0.09 vs 0.06). Our gradient observations are in alignment with measurement over temperate
332 grasslands (-0.40 to 0.27 ng m^{-4}) (Fritsche et al., 2008b).

Basic statistics of the MM Hg^0 flux observations is presented in Table 1. The variability in our
334 observations is similar with those reported from previous studies using MM-flux measurement technique
over uncontaminated croplands (corn, soybean and rice paddy fields) (Baya and Van Heyst, 2010; Cobos
336 and Baker, 2002; Kim et al., 2003; Cobbett and Van Heyst, 2007). The MM fluxes exhibited strong temporal
variability during daytime and much weaker variability under low quality turbulence during nighttime. In a
338 typical campaign day, the turbulent flux datasets included both periods of emission and dry deposition. The median
of nighttime flux was much smaller than the daytime flux for all MM methods (Mann-Whitney U-test, MBR and
340 AGM $p < 0.001$, $p < 0.10$ for REA).

The distribution of the turbulent fluxes and Hg^0 concentration gradient in Fig. 4 deviated significantly
342 from Gaussian distribution in Hg^0 concentration gradient and in the derived MBR and AGM fluxes
(Shapiro-Wilk's test rejected the hypothesis of normality of the distributions, $p < 0.01$). The statistical MM
344 fluxes (median \pm MAD) in IC #1 (Fig. 7A) were -0.5 ± 8.9 and $0.1 \pm 3.2 \text{ ng m}^{-2} \text{ h}^{-1}$ for AGM and MBR
measurement, while 2.8 ± 29.0 , 1.4 ± 15.2 , and $8.8 \pm 45.3 \text{ ng m}^{-2} \text{ h}^{-1}$ for AGM, MBR and REA in IC #2 (Fig.
346 7B), respectively. All the distributions of MM turbulent flux were associated with a positive kurtosis (3.8 -
16.2) and a slightly positive skewness (0.8 - 1.5). The observed flux frequency distributions for AGM and
348 MBR peaked more strongly than that of REA (Fig. 7), with the MBR method giving the most confined

distribution. Broader flux distribution measured by REA sampling method has been reported in the
350 measurements of turbulent fluxes for other gases (Fowler et al., 1995;Beverland et al., 1996;Nemitz et al.,
2001). Previous studies suggest that vegetation canopy in growing stage acts an Hg⁰ sink by net uptake of
352 Hg⁰ into foliage and therefore contributes to dry depositional flux (Bash and Miller, 2009;Stamenkovic and
Gustin, 2007). However, the three MM-techniques in this study derived significant higher average Hg⁰
354 emission fluxes in IC #2 compared to IC #1, indicating the vegetation sink strength was not sufficient to
offset the efflux from underlying soil surface for croplands. Even though not measured, it is credible to
356 assume that the soil Hg⁰ efflux was higher during the warmer IC#2 due to higher temperature (Table 1)
(Baya and Van Heyst, 2010;Gustin, 2011).

358

3.3.2 Comparison of Hg⁰ fluxes derived from micrometeorological methods

360 The larger variability in REA- compared to the gradient-derived fluxes is associated with a
combination of methodological, instrumental and site-specific constraints influencing primarily the
362 resolution of ΔC_{REA} (Eq. 3) as identified and discussed in Part II of this paper series (Zhu et al., 2014a).
Nevertheless, a Friedman two-way analysis of variance by ranks (a non-parametric method) showed that the
364 median fluxes by the three MM methods were not significantly different ($\chi^2 = 1.29 < \chi^2_{p=0.05} = 5.99$).
This indicated that AGM, MBR and REA methods produced comparable results with respect to the median
366 location of Hg⁰ turbulent flux during the inter-comparison.

The MBR method relies on scalar similarity (similarity in the scalar time series throughout the scalar spectra,
368 Kaimal et al., 1972) between Hg⁰ and temperature used as the proxy in this study. Since we have no means of
explicitly characterizing Hg⁰ scalar spectra, it is important to address the distribution of sources and sinks within
370 the footprint area (Foken, 2008). By choosing a large flat and uniform fetch with confined Hg content in the soil

substrate, significant divergence from scalar similarity between Hg^0 and temperature is less likely to occur.

372 Nevertheless, non-stationary effects (e.g. [advection of Hg polluted air-masses and related changes in concentration with time](#)) bias the measured turbulent flux in relation to the actual air-surface exchange process (See Section 3.4).

374 The MBR method becomes uncertain and may significantly overestimate flux when the numerator and denominator in the formula of eddy diffusivity approaching small numbers, which typically occur in periods at dawn, dusk and during nighttime (Eq. 6, c.f. [Converse et al., 2012](#)). As shown in [Fig. 8](#), the 20-min averaged

376 AGM- and MBR-derived fluxes were well correlated during both campaigns (slope = 0.76 and 0.86). **However,** when the sensible heat flux becomes small (small temperature gradient) at $|H| < 20 \text{ W m}^{-2}$, the correlation coefficient diminishes drastically and the fall-off in slope ($F_{AGM} / F_{MBR} = 0.35 - 0.36$) implying that the MBR

378 method can significant overestimate turbulent Hg^0 fluxes. MBR flux data collected in the presence of small scalar gradients (often during dawn and dusk transition periods) are therefore of questionable quality and should be

380 considered for omission.

AGM fluxes were on an average 26.1% lower than MBR fluxes during IC #1, but 13.8% higher during IC #2.

384 The disparate results may largely stem from methodological issues ([Fritsche et al., 2008b](#)). In some previous studies using the AGM method to gauge various trace gas fluxes including Hg^0 ([Edwards et al., 2001](#); [Edwards et al., 2005](#); [Simpson et al., 1997](#)), normalization of Eq. 5 was introduced to mitigate for systematical failure of obtaining energy budget closures ([Twine et al., 2000](#)) by a factor of 1.3 - 1.35. The AGM method involves

386 momentum flux, and an atmospheric stability parameterization in the flux calculation. For conditions of weak developed turbulence to a greater extent prevailing under nocturnal stable stratification, where u_* is very low, the

388 AGM and MBR methods are prone to large uncertainties and corresponding fluxes are suggested to be flagged by applying wind or friction velocity thresholds (viz. $u_* < 0.07 - 0.1 \text{ m s}^{-1}$) ([Fritsche et al., 2008b](#); [Foken, 2008](#)).

390 During IC#2, when the REA-system was included, the agreement between REA and the gradient-based methods

392

was worst for small fluxes, which is inherently connected with the lower precision of the former system. As to be
394 discussed in [Zhu et al. 2014a](#), the non-constant (i.e. concentration and time dependent) sampling channel bias,
which is difficult to entirely account for, [is relatively](#) more aggravating for the REA approach. [Other gases \(e.g.](#)
396 [NH₃, CH₄\)](#) that have been studied with this triad of MM-techniques, higher variability in REA flux is generically
observed ([Nemitz et al., 2001](#); [Fowler et al., 1995](#); [Moncrieff et al., 1998](#)). In addition, systematically fluxes
398 differences between a suite of [NH₃-REA](#) systems as well as collocated AGM system inter-compared have been
reported ([Hensen et al., 2009](#)).

400

3.4 Comparison of chamber and micrometeorological techniques

402 3.4.1 *Footprint of flux measurement*

While the footprint ([enclosed soil surface](#)) of the chamber methods is fixed and very small (0.06 m²
404 for TDFC and 0.09 m² for NDFC), MM methods derive fluxes from a footprint of comparatively large
spatial extension upwind the sampling tower. [The MM-footprint is not constant over time but a complex](#)
406 [function of the sensor height, surface roughness length and canopy structure together with changing](#)
[meteorological conditions.](#) The predicted source area ([using the models of Kljun et al., 2004 and Kormann](#)
408 [and Meixner, 2001](#)) tends for upper sampling level ($z_2 = z_{REA}$) to be extensive for flux periods associated
with weakly developed turbulence (Flag 2). In the contrast, ~70% and ~86% of the data cleared for good
410 turbulence quality, $\hat{x}_{70\%}$ (along-wind distance providing 70% cumulative contribution to turbulent flux)
fall within the unbroken field (150 m) for IC #1 and IC #2 respectively. For the lower sampling height (z_1),
412 the footprint falls almost entirely within the primary fetch. Nevertheless, heterogeneous structures (roads,
streams, tree stands and low buildings) existing outside the primary fetch (>150 m) are of minor spatial
414 extent and within a radius of ~2 km, the sampling tower can be regarded to be surrounded by unbroken

farmlands.

416

3.4.2 *Diel variations*

418 [Fig. 9](#) shows boxplots of the diurnal variation of Hg^0 flux obtained by the five examined methods.

Consistent in both campaigns, the MM methods exhibited highly variable fluxes, especially during daytime,

420 where the magnitude in a single 20-min turbulent flux can exceed the flux derived by the chamber methods

by many times. [DFCs fluxes followed a well-defined diurnal pattern with consistent daytime emission and](#)

422 [slight nighttime deposition. The pattern is similar to those for solar irradiance and temperature and reflects](#)

[that the air-soil \$\text{Hg}^0\$ flux derived from DFC-technique is primarily governed by thermal and light-induced](#)

424 [controls \(e.g. Bahlmann et al., 2006\). On the contrary, flux from MM measurements is subject to the](#)

[constant changes of atmospheric turbulence within the planetary boundary layer.](#) To facilitate a comparison

426 between the DFC and MM data set on a diurnal basis, a Savitzky-Golay filter was applied on

hourly-averaged turbulent Hg^0 flux data to smooth out the short-term variability. In [Fig.10](#), where the

428 diurnal courses of flux are given by smoothing spline fits, there is a 2-hr lag in the time of the day when

turbulent and chamber-derived flux peaked (IC #1). For the DFCs, the observed Hg^0 flux peaked within the

430 period P2 ([Fig. 10, IC #1](#)) in concert with soil temperature, which is consistent with diurnal cycles reported

for chamber measurements in the literatures ([Fu et al., 2008;Fu et al., 2012;Gustin, 2011;Zhu et al., 2013a](#)).

432 The smoothed mean diurnal cycle derived by the gradient-based methods over the same period

exhibits peaking Hg^0 [fluxes shortly before](#) mid-day (P1 in [Fig. 10, IC #1](#)) but also include a subsequent

434 shoulder in the flux profile in the early afternoon (within P2 in [Fig. 10, IC #1](#)). The pattern resembles to

extent that of latent heat flux (evapotranspiration) ([Liu and Foken, 2001](#)) and may be interpreted as an

436 effect of photo-reduction of previously deposited Hg^{II} to Hg^0 into soil in conjunction with the presence of a

water film (frost and dewfall) and emerging incoming solar radiation and temperature-driven air-surface
438 exchange of soil Hg⁰ pool (Fritsche et al., 2008b). Nevertheless, measurement of air-surface Hg⁰ fluxes
under the marked varying Hg⁰ concentrations in air is challenging. Under such conditions, the measured
440 turbulent fluxes are altered by non-stationary bias thus they do not represent actual fluxes to surface. The
rates of change in Hg⁰ concentration (up to ~ ±1.1 ng m⁻³ h⁻¹) at the storage height of nearly 3 m relevant to
442 this study imply vertical Hg⁰ flux divergence in the range ±3 ng m⁻² h⁻¹. At low turbulence, advection in
addition may as well gain some importance. However, to fully quantify the advection term for Hg⁰ requires
444 an array of instrumentation and such an investigation was unfeasible to accomplish in this study.

The mean diurnal cycles calculated for the three coevally examined MM methods (Fig. 10, IC #2) are
446 based on a significantly smaller set of input data (~30% of IC #1) and therefore plausibly less robust to
provide adequate representativeness after smoothing. Moreover, the campaign is a composite of periods
448 where near-neutral conditions prevailed on daytime as well as adjacent nights and periods with weakly
developed turbulence during night-time respectively. Accordingly, the MM methods unanimously gauged
450 maximum fluxes slightly after noon-time (P2, IC #2). However, there are features (P1 & P3) in the
constructed cycles that are difficult to fully couple to environmental responses.

452

3.4.3 Comparison of Hg⁰ flux and deposition velocity derived from different methods

454 The overall correlation matrix between Hg⁰ flux, ambient Hg⁰ concentration and other measured
parameters (hourly averages) are displayed in Table 2. The fluxes derived from the two types of chambers
456 were highly positively correlated ($R=0.95$, $p < 0.01$). Among the MM methods, MBR and AGM fluxes
were well correlated, while REA fluxes were not significantly correlated with fluxes derived by other
458 techniques ($R < 0.2$, $p > 0.05$). A significant correlation was observed between DFCs and gradient fluxes (R

~0.5 for DFCs and AGM). Using the dry deposition velocity (V_d) calculation in Poissant et al. (2004), the median Hg^0 deposition velocity (dry deposition events) inferred from different measurement methods were 0.01 $cm\ s^{-1}$ (MBR, 47%) < 0.03 $cm\ s^{-1}$ (TDFC, 56%) < 0.04 $cm\ s^{-1}$ (NDFC, 59%) < 0.06 $cm\ s^{-1}$ (AGM, 56%) and 0.09 $cm\ s^{-1}$ (AGM, 34%) < 0.13 $cm\ s^{-1}$ (MBR, 36%) < 0.20 $cm\ s^{-1}$ (REA, 36%) for IC #1 and IC #2, respectively. The observed Hg^0 dry deposition velocities from the two campaigns are in good agreement with the V_d of previous measurements over background soil (DFCs methods, generally < 0.05 $cm\ s^{-1}$) and agricultural canopies (MM methods, 0.05 – 0.28 $cm\ s^{-1}$) (Zhang et al., 2009 and references there in).

The cumulative flux derived by the examined methods is presented in Fig. 11A&B. During IC #1, the cumulative fluxes measured by MBR and AGM fell between the fluxes measured by the two DFC methods. A period of divergence in the magnitude between the derived turbulent exchange parameters (eddy diffusivity of heat and ν_{tr}) resulted in intersected courses of MBR and AGM cumulative flux (17th Nov.). MBR flux then stayed beyond the AGM flux on a cumulative basis for the rest of the campaign. The cumulative flux gauged by the TDFC method was the lowest (approximately 1/3 of MBR flux). Over the duration of IC #1, the net Hg^0 flux estimated by MBR and NDFC method was in good agreement (2.90 vs. 3.02 $\mu g\ m^{-2}$) while the AGM method derived ~25% lower Hg^0 net evasion. This indicated that the flux correction with synchronized surface shear properties in NDFC partially bridges frequently observed disparities in magnitude between the MM- and conventional chamber-derived fluxes (e.g. Gustin et al., 1999). Fig. 12A show scatterplots of hourly flux specifically for MBR versus NDFC/TDFC, the correlation between individual hourly data points is weak. While in the Fig 12B, the deviation between MBR cumulative fluxes and NDFC/TDFC cumulative fluxes during the sampling campaign suggest NDFC measurement show a great advantage in bridge the flux gap between DFCs and MBR measurement. The

significant scattering in Fig. 12A stems substantially from the inherent high variability in MBR flux
482 prevalent during daytime. The difference between chamber and MBR flux depends to certain degree on the
diurnal variation of the atmospheric conditions. During day-time, the chamber produces a delay in the
484 day-time flux evolution and fluxes become sustained in the late afternoon due to an artificial reduction in
surface cooling within the chamber (Fig. 10).

486 During IC #2, the gradient-based MM techniques were evaluated together with the REA technique.
The temporally features of the convoluted MBR and AGM cumulative fluxes are by large concordant
488 albeit the latter technique gauged ~20% higher Hg^0 net flux (1.78 vs. 1.43 $\mu\text{g m}^{-2}$). The relative magnitude
of MBR and AGM flux shown inverse order during the two campaigns, possibly caused by methodological
490 limitations given by the diverging micro-meteorological conditions (Zhu et al., 2014a). For an extended period,
the cumulative flux of REA given in Fig. 11B evolved in a similar way to those of the gradient-based
492 methods (18th – 21st Apr). However, considerably different fluxes, occasionally in reverse directions
occurred after 21st Apr. In particularly during 16th – 17th April (Fig. 11B), a large net emission event was
494 observed by all three techniques but at different magnitude.

496 3.5 Correlation between Hg^0 flux observation and environmental factors

It has been shown that the air-surface exchange of Hg can be influenced by solar irradiation,
498 temperature, humidity, moisture, wind shear condition, and biotic processes (Choi and Holsen,
2009; Eckley et al., 2010; Fu et al., 2008; Gustin, 2011; Zhu et al., 2013a; Lin et al., 2010), as also observed
500 in our field (Fig. 9 and Fig. 10). Table 2 shows the Pearson correlation coefficients between Hg^0 fluxes
measured by the different methods and meteorological variables. DFC Hg^0 fluxes were positively
502 correlated with solar radiation, soil temperature, soil moisture, friction velocity ($R \sim 0.4 - 0.9$, $p < 0.05$),

and negatively correlated with air Hg^0 concentration and air humidity ($p < 0.05$). The correlations between
504 the MM fluxes and environmental variables were generally weaker ($|R| < 0.5$) in both campaigns. It is
evident that DFC is less sensitive to surrounding atmospheric conditions that control the MM flux. On the
506 contrary, the Hg^0 flux controls in the ecosystem enclosed by the chamber are subject to its
microenvironment conditions that are significantly perturbed foremost by solar heating.

508

4. Conclusions and Implications

510 In this study, we performed a comprehensive inter-comparison of five contemporary Hg^0 flux
quantification techniques through collocated measurements over an agricultural field. The flat terrain and
512 homogeneous soil Hg content at the experimental site are ideal for the inter-comparison of the DFCs and
MM techniques. MM- and DFC-derived Hg^0 fluxes showed distinct temporal characteristics. The former
514 exhibited a highly dynamic variability while the latter had gradual temporal features. Diurnal trends
showed that MM- and DFC-measurement diagnosed a similar daytime emission peak with different
516 peaking times. Such differences were driven by separate sets of environmental factors influencing the DFC
(irradiance and temperature) and MM (atmospheric turbulence properties) measurements. The three MM
518 methods (REA, AGM and MBR) observed statistically significant, inseparable median Hg^0 fluxes ($p <$
0.05) albeit REA flux was distributed over a much broader scale. Gradient and DFCs methods
520 inter-compared favorably with respect to the confined location of median fluxes. Instantaneous fluxes
measured by NDFC and TDFC and by MBR and AGM methods respectively were highly correlated ($R >$
522 0.8, $p < 0.05$) as the pairwise techniques are based on same theoretical concept. However, the
comparability between individual DFC and MM fluxes was poor to moderate ($R \sim 0.1 - 0.5$) indicating the
524 risk of utilizing sporadic (non-diurnally resolved) flux measurements as representative of an ecosystem.

The five techniques gauged unanimously positive net Hg^0 fluxes cumulated over the campaign
526 periods. For the investigated triad of MM-techniques, Hg^0 -REA system has a general tendency to derive
fluxes largest in magnitude. Over most of the campaign time, REA reported 20 - 60% higher cumulative
528 flux compared to the AGM method next to REA. Intriguingly, the Hg^0 flux budget magnitude examined by
AGM and MBR methods was reversed during the two campaigns with a difference of ~20%, which may
530 result from the atmospheric conditions and proxy scalar behavior. The traditional DFC method
systematically measured the lowest Hg^0 net emission (42% and 31% of AGM- and MBR-derived net
532 emission, respectively). The NDFC technique measured averaged fluxes similar to turbulent Hg^0 fluxes
obtained by the MBR method (5.3% difference). Although not entirely coupled to the atmospheric
534 conditions that control the flux, the NDFC technique nevertheless represents a significant progress and
improvement in contemporary enclosure-based Hg^0 flux measurement.

536 It was feasible to obtain a gradient measurement height ratio at the recommended bound (Foken,
2008). Given the lower precision of REA, gradient-based methods is consequently to recommend for
538 atmosphere-ecosystem Hg^0 flux measurements over low vegetation. REA has its niche over tall canopy,
where gradient methods have frequently been found impracticable. In future applications, concerning
540 foremost MM flux measurement technique, where the capacity to resolve small concentration differences
is critical, it is recommended to implement analysis of synchronously collected samples for various heights
542 (AGM, MBR) and conditionally segregated air parcels (REA) to avoid uncertainties induced by
non-uniform ambient air Hg^0 concentration during the flux averaging period. It has recently been argued
544 that direct measurement of Hg^0 ecosystem air-canopy gas exchange is difficult and potential subject to
larger uncertainties (Zhang et al., 2012). Nevertheless, it is practicable for Hg^0 as it is for other trace gases
546 and aerosols for which continuous MM-flux measurement systems are key tools in ecosystem sciences.

Our results show that improvement in resolving small Hg^0 concentration differences for the MM-systems
548 is required to further reduce uncertainties in the flux estimation.

550 *Acknowledgements*

This research was financially supported by “973 Program” (2013CB430002), National Science Foundation
552 of China (41030752), Chinese Academy of Sciences through an instrument development program
(YZ200910), and the State Key Laboratory of Environmental Geochemistry. We would thank the staff
554 from Yucheng Comprehensive Experimental Station, Chinese Academy of Sciences for their sampling
assistance.

556

558 **References**

- 560 Aubinet, M., Vesala, T., and Papale, D.: Eddy covariance: a practical guide to measurement and data analysis,
Springer, 2012.
- 562 [Bahlmann, E., Ebinghaus, R., and Ruck, W.: Development and application of a laboratory flux
measurement system \(LFMS\) for the investigation of the kinetics of mercury emissions from soils, *Journal
564 of Environmental Management*, 81, 114-125, 2006.](#)
- Bash, J. O., and Miller, D. R.: A relaxed eddy accumulation system for measuring surface fluxes of total gaseous
566 mercury, *Journal of Atmospheric and Oceanic Technology*, 25, 244-257, 2008.
- Bash, J. O., and Miller, D. R.: Growing season total gaseous mercury (TGM) flux measurements over an *Acer
568 rubrum* L. stand, *Atmospheric Environment*, 43, 5953-5961, 2009.
- Bash, J. O.: Description and initial simulation of a dynamic bidirectional air-surface exchange model for
570 mercury in Community Multiscale Air Quality (CMAQ) model, *Journal of Geophysical Research-Atmospheres*,
115, 2010.
- 572 Baya, A. P., and Van Heyst, B.: Assessing the trends and effects of environmental parameters on the behaviour
of mercury in the lower atmosphere over cropped land over four seasons, *Atmos. Chem. Phys.*, 10, 8617-8628,
574 2010.
- Beverland, I. J., Oneill, D. H., Scott, S. L., and Moncrieff, J. B.: Design, construction and operation of flux
576 measurement systems using the conditional sampling technique, *Atmospheric Environment*, 30, 3209-3220,
1996.
- 578 Carpi, A., and Lindberg, S. E.: Application of a Teflon (TM) dynamic flux chamber for quantifying soil mercury
flux: Tests and results over background soil, *Atmospheric Environment*, 32, 873-882, 1998.

580 Cobbett, F. D., and Van Heyst, B. J.: Measurements of GEM fluxes and atmospheric mercury concentrations
 (GEM, RGM and Hg-P) from an agricultural field amended with biosolids in Southern Ont., Canada (October
 582 2004-November 2004), *Atmospheric Environment*, 41, 2270-2282, 2007.

Cobos, D. R., and Baker, J. M.: Conditional sampling for measuring mercury vapor fluxes, *Atmospheric*
 584 *Environment*, 36, 4309-4321, 2002.

Converse, A. D., Riscassi, A. L., and Scanlon, T. M.: Seasonal variability in gaseous mercury fluxes measured in
 586 a high-elevation meadow, *Atmospheric Environment*, 44, 2176-2185, 2010.

Durnford, D., Dastoor, A., Figueras-Nieto, D., and Ryjkov, A.: Long range transport of mercury to the Arctic and
 588 across Canada, *Atmos. Chem. Phys.*, 10, 6063-6086, 2010.

Eckley, C. S., Gustin, M., Lin, C. J., Li, X., and Miller, M. B.: The influence of dynamic chamber design and
 590 operating parameters on calculated surface-to-air mercury fluxes, *Atmospheric Environment*, 44, 194-203, 2010.

Edwards, G. C., Rasmussen, P. E., Schroeder, W. H., Kemp, R. J., Dias, G. M., Fitzgerald-Hubble, C. R., Wong,
 592 E. K., Halfpenny-Mitchell, L., and Gustin, M. S.: Sources of variability in mercury flux measurements, *Journal*
of Geophysical Research-Atmospheres, 106, 5421-5435, 2001.

Edwards, G. C., Rasmussen, P. E., Schroeder, W. H., Wallace, D. M., Halfpenny-Mitchell, L., Dias, G. M., Kemp,
 594 R. J., and Ausma, S.: Development and evaluation of a sampling system to determine gaseous Mercury fluxes
 596 using an aerodynamic micrometeorological gradient method, *Journal of Geophysical Research-Atmospheres*,
 110, doi:10.1029/2004jd005187, 2005.

Farmer, D. K., Wooldridge, P. J., and Cohen, R. C.: Application of thermal-dissociation laser induced
 598 fluorescence (TD-LIF) to measurement of HNO₃, Σ alkyl nitrates, Σ peroxy nitrates, and NO₂ fluxes using eddy
 600 covariance, *Atmos. Chem. Phys.*, 6, 3471-3486, 2006.

Feng, X. B., Wang, S. F., Qiu, G. L., Hou, Y. M., and Tang, S. L.: Total gaseous mercury emissions from soil in
 602 Guiyang, Guizhou, China, *Journal of Geophysical Research-Atmospheres*, 110, 2005.

Foken, T.: *Micrometeorology*, Springer-Verlag, Berlin, Heidelberg, 306 pp., 2008.

604 Fowler, D., Hargreaves, K. J., Skiba, U., Milne, R., Zahniser, M. S., Moncrieff, J. B., Beverland, I. J., and
 Gallagher, M. W.: Measurements of CH₄ and N₂O fluxes at the landscape scale using micrometeorological
 606 methods, *Philosophical Transactions: Physical Sciences and Engineering*, 351, 339-355, 1995.

Fritsche, J., Obrist, D., Zeeman, M. J., Conen, F., Eugster, W., and Alewell, C.: Elemental mercury fluxes over a
 608 sub-alpine grassland determined with two micrometeorological methods, *Atmospheric Environment*, 42,
 2922-2933, 2008a.

610 Fritsche, J., Wohlfahrt, G., Ammann, C., Zeeman, M., Hammerle, A., Obrist, D., and Alewell, C.: Summertime
 elemental mercury exchange of temperate grasslands on an ecosystem-scale, *Atmos. Chem. Phys.*, 8, 7709-7722,
 612 2008b.

Fu, X., Feng, X., Zhang, H., Yu, B., and Chen, L.: Mercury emissions from natural surfaces highly impacted by
 614 human activities in Guangzhou province, South China, *Atmospheric Environment*, 46, 185-193, 2012.

Fu, X. W., Feng, X. B., and Wang, S. F.: Exchange fluxes of Hg between surfaces and atmosphere in the eastern
 616 flank of Mount Gongga, Sichuan province, southwestern China, *Journal of Geophysical Research-Atmospheres*,
 113, 2008.

618 Fu, X. W., Feng, X. B., Wan, Q., Meng, B., Yan, H. Y., and Guo, Y. N.: Probing Hg evasion from surface waters
 of two Chinese hyper/meso-eutrophic reservoirs, *Science of the Total Environment*, 408, 5887-5896, 2010.

620 Gustin, M., and Jaffe, D.: Reducing the Uncertainty in Measurement and Understanding of Mercury in the
 Atmosphere, *Environ. Sci. Technol.*, 44, 2222-2227, 2010.

622 Gustin, M. S., Lindberg, S., Marsik, F., Casimir, A., Ebinghaus, R., Edwards, G., Hubble-Fitzgerald, C., Kemp,
 R., Kock, H., Leonard, T., London, J., Majewski, M., Montecinos, C., Owens, J., Pilote, M., Poissant, L.,

624 Rasmussen, P., Schaedlich, F., Schneeberger, D., Schroeder, W., Sommar, J., Turner, R., Vette, A., Wallschlaeger,
D., Xiao, Z., and Zhang, H.: Nevada STORMS project: Measurement of mercury emissions from naturally
626 enriched surfaces, *Journal of Geophysical Research-Atmospheres*, 104, 21831-21844, 1999.

Gustin, M. S., and Lindberg, S. E.: Assessing the contribution of natural sources to the global mercury cycle:
628 The importance of intercomparing dynamic flux measurements, *Fresenius' Journal of Analytical Chemistry*, 366,
417-422, 2000.

630 Gustin, M. S.: Exchange of mercury between the atmosphere and terrestrial ecosystems, in: *Environmental
Chemistry and Toxicology of Mercury*, edited by: Liu, G. L., Cai, Y., and O'Driscoll, N., 423-451, 2011.

632 Hensen, A., Nemitz, E., Flynn, M., Blatter, A., Jones, S., Sørensen, L. L., Hensen, B., Pryor, S., Jensen, B., and
Otjes, R.: Inter-comparison of ammonia fluxes obtained using the Relaxed Eddy Accumulation technique,
634 *Biogeosciences*, 6, 2575-2588, 2009.

Hou, R., Ouyang, Z., Li, Y., Tyler, D. D., Li, F., and Wilson, G. V.: Effects of tillage and residue management on
636 soil organic carbon and total nitrogen in the North China Plain, *Soil Science Society of America Journal*, 76,
230-240, 2012.

638 Kaimal, J., Wyngaard, J., Izumi, Y., and Coté O.: Spectral characteristics of surface-layer turbulence, *Quarterly
Journal of the Royal Meteorological Society*, 98, 563-589, 1972.

640 Kim, K. H., Kim, M. Y., Kim, J., and Lee, G.: Effects of changes in environmental conditions on atmospheric
mercury exchange: Comparative analysis from a rice paddy field during the two spring periods of 2001 and
642 2002, *Journal of Geophysical Research-Atmospheres*, 108, 2003.

Li, Z. G., Feng, X., Li, P., Liang, L., Tang, S. L., Wang, S. F., Fu, X. W., Qiu, G. L., and Shang, L. H.: Emissions
644 of air-borne mercury from five municipal solid waste landfills in Guiyang and Wuhan, China, *Atmos. Chem.
Phys.*, 10, 3353-3364, 2010.

646 Lin, C.-J., Zhu, W., Li, X., Feng, X., Sommar, J., and Shang, L.: Novel dynamic flux chamber for measuring
air-surface exchange of Hg⁰ from soils, *Environ. Sci. Technol.*, 46, 8910-8920, 2012.

648 Lin, C.-J., Gustin, M. S., Singhasuk, P., Eckley, C., and Miller, M.: Empirical models for estimating mercury
flux from soils, *Environ. Sci. Technol.*, 44, 8522-8528, 2010.

650 Lindberg, S. E., Kim, K. H., Meyers, T. P., and Owens, J. G.: Micrometeorological gradient approach for
quantifying air-surface exchange of mercury-vapor - tests over contaminated soils, *Environ. Sci. Technol.*, 29,
652 126-135, 1995.

Lindqvist, O., Johansson, K., Bringmark, L., Timm, B., Aastrup, M., Andersson, A., Hovsenius, G., Håkanson,
654 L., Iverfeldt, Å., and Meili, M.: Mercury in the Swedish environment — Recent research on causes,
consequences and corrective methods, *Water, Air, and Soil Pollution*, 55, xi-261, 10.1007/BF00542429, 1991.

656 Liu, H., and Foken, T.: A modified Bowen ratio method to determine sensible and latent heat fluxes,
Meteorologische Zeitschrift, 10, 71-80, 2001.

658 Marsik, F. J., Keeler, G. J., Lindberg, S. E., and Zhang, H.: Air-surface exchange of gaseous mercury over a
mixed sawgrass-cattail stand within the Florida Everglades, *Environ. Sci. Technol.*, 39, 4739-4746, 2005.

660 Mauder, M., Cuntz, M., Drüe, C., Graf, A., Rebmann, C., Schmid, H. P., Schmidt, M., and Steinbrecher, R.: A
strategy for quality and uncertainty assessment of long-term eddy-covariance measurements, *Agricultural and
662 Forest Meteorology*, 169, 122-135, 2013.

Moncrieff, J. B., Beverland, I. J., ÓNáil, D. H., and Cropley, F. D.: Controls on trace gas exchange observed by
664 a conditional sampling method, *Atmospheric Environment*, 32, 3265-3274, 1998.

Monin, A., and Obukhov, A.: Basic laws of turbulent mixing in the surface layer of the atmosphere, *Contrib.
666 Geophys. Inst. Acad. Sci. USSR*, 151, 163-187, 1954.

[National Atmospheric Deposition Program \(NADP\): Atmospheric Mercury Network Operations Manual](#)

668 (2011–05) Version 1.0., http://nadp.isws.illinois.edu/amn/docs/AMNet_Operations_Manual.pdf, NADP Program
Office, 2204 Griffith Dr., Champaign, IL 61820, 2011.

670 Nemitz, E., Flynn, M., Williams, P., Milford, C., Theobald, M., Blatter, A., Gallagher, M., and Sutton, M.: A
672 relaxed eddy accumulation system for the automated measurement of atmospheric ammonia fluxes, *Water, Air
and Soil Pollution: Focus*, 1, 189-202, 2001.

Nemitz, E., Loubet, B., Lehmann, B. E., Cellier, P., Neftel, A., Jones, S. K., Hensen, A., Ihly, B., Tarakanov, S.
674 V., and Sutton, M. A.: Turbulence characteristics in grassland canopies and implications for tracer transport,
Biogeosciences, 6, 1519-1537, 2009.

676 Olofsson, M., Sommar, J., Ljungström, E., and Andersson, M.: Application of relaxed eddy accumulation
techniques to qualify Hg⁰ fluxes over modified soil surfaces, *Water Air Soil Poll*, 167, 331-354, 2005.

678 Panofsky, H. A., and Dutton, J. A.: Atmospheric turbulence, models and methods for engineering applications,
John Wiley & Sons, New York, 1984.

680 Park, J.-H., Goldstein, A., Timkovsky, J., Fares, S., Weber, R., Karlik, J., and Holzinger, R.: Active
atmosphere-ecosystem exchange of the vast majority of detected volatile organic compounds, *Science*, 341,
682 643-647, 2013.

Pirrone, N., Cinnirella, S., Feng, X., Finkelman, R. B., Friedli, H. R., Leaner, J., Mason, R., Mukherjee, A. B.,
684 Stracher, G. B., Streets, D. G., and Telmer, K.: Global mercury emissions to the atmosphere from anthropogenic
and natural sources, *Atmos. Chem. Phys.*, 10, 5951-5964, 2010.

686 Poissant, L., and Casimir, A.: Water-air and soil-air exchange rate of total gaseous mercury measured at
background sites, *Atmospheric Environment*, 32, 883-893, 1998.

688 Poissant, L., Pilote, M., and Casimir, A.: Mercury flux measurements in a naturally enriched area: Correlation
with environmental conditions during the Nevada Study and Tests of the Release of Mercury From Soils
690 (STORMS), *Journal of Geophysical Research-Atmospheres*, 104, 21845-21857, 1999.

Poissant, L., Pilote, M., Xu, X. H., Zhang, H., and Beauvais, C.: Atmospheric mercury speciation and deposition
692 in the Bay St. Francois wetlands, *Journal of Geophysical Research-Atmospheres*, 109, 2004.

Simpson, I., Edwards, G., Thurtell, G., Den Hartog, G., Neumann, H., and Staebler, R.: Micrometeorological
694 measurements of methane and nitrous oxide exchange above a boreal aspen forest, *Journal of Geophysical
Research: Atmospheres*, 102, 29331-29341, 1997.

696 Sommar, J., Zhu, W., Lin, C.-J., and Feng, X.: Field approaches to measure Hg exchange between natural
surfaces and the atmosphere - a review, *Critical Reviews in Environmental Science and Technology*, 43,
698 1657-1739, 2013a.

Sommar, J., Zhu, W., Shang, L., Feng, X., and Lin, C.-J.: A whole-air relaxed eddy accumulation measurement
700 system for sampling vertical vapour exchange of elemental mercury, *Tellus B*, 65, 19940, 2013b.

Stamenkovic, J., and Gustin, M. S.: Evaluation of use of EcoCELL technology for quantifying total gaseous
702 mercury fluxes over background substrates, *Atmospheric Environment*, 41, 3702-3712, 2007.

Twine, T. E., Kustas, W., Norman, J., Cook, D., Houser, P., Meyers, T., Prueger, J., Starks, P., and Wesely, M.:
704 Correcting eddy-covariance flux underestimates over a grassland, *Agricultural and Forest Meteorology*, 103,
279-300, 2000.

706 Walker, J., Robarge, W., Wu, Y., and Meyers, T.: Measurement of bi-directional ammonia fluxes over soybean
using the modified Bowen-ratio technique, *Agricultural and Forest Meteorology*, 138, 54-68, 2006.

708 Wallschläger, D., Turner, R. R., London, J., Ebinghaus, R., Kock, H. H., Sommar, J., and Xiao, Z. F.: Factors
affecting the measurement of mercury emissions from soils with flux chambers, *Journal of Geophysical
710 Research-Atmospheres*, 104, 21859-21871, 1999.

Wang, S. F., Feng, X. B., Qiu, G. L., Wei, Z. Q., and Xiao, T. F.: Mercury emission to atmosphere from

712 Lanmuchang Hg-Tl mining area, Southwestern Guizhou, China, *Atmospheric Environment*, 39, 7459-7473,
2005.

714 Wang, S. F., Feng, X. B., Qiu, G. L., Fu, X. W., and Wei, Z. Q.: Characteristics of mercury exchange flux
716 between soil and air in the heavily air-polluted area, eastern Guizhou, China, *Atmospheric Environment*, 41,
5584-5594, 2007.

Wesely, M. L., and Hicks, B. B.: A review of the current status of knowledge on dry deposition, *Atmospheric*
718 *Environment*, 34, 2261-2282, 2000.

Whitehead, J. D., Twigg, M., Famulari, D., Nemitz, E., Sutton, M. A., Gallagher, M. W., and Fowler, D.:
720 Evaluation of Laser Absorption Spectroscopic Techniques for Eddy Covariance Flux Measurements of
Ammonia, *Environ. Sci. Technol.*, 42, 2041-2046, 2008.

722 Xiao, Z. F., Munthe, J., Schroeder, W. H., and Lindqvist, O.: Vertical Fluxes of Volatile Mercury over Forest Soil
and Lake Surfaces in Sweden, *Tellus B*, 43, 267-279, 1991.

724 Zhang, H., Lindberg, S. E., Barnett, M. O., Vette, A. F., and Gustin, M. S.: Dynamic flux chamber measurement
of gaseous mercury emission fluxes over soils. Part 1: simulation of gaseous mercury emissions from soils using
726 a two-resistance exchange interface model, *Atmospheric Environment*, 36, 835-846, 2002.

Zhang, L., Blanchard, P., Gay, D. A., Prestbo, E. M., Risch, M. R., Johnson, D., Narayan, J., Zsolway, R.,
728 Holsen, T. M., Miller, E. K., Castro, M. S., Graydon, J. A., Louis, V. L. S., and Dalziel, J.: Estimation of
speciated and total mercury dry deposition at monitoring locations in eastern and central North America, *Atmos.*
730 *Chem. Phys.*, 12, 4327-4340, 2012.

Zhang, L., Wang, S. X., Wang, L., and Hao, J. M.: Atmospheric mercury concentration and chemical speciation
732 at a rural site in Beijing, China: implications of mercury emission sources, *Atmos. Chem. Phys.*, 13,
10505-10516, 2013.

734 Zhu, W., Li, Z., Chai, X., Hao, Y., Lin, C.-J., Sommar, J., and Feng, X.: Emission characteristics and air-surface
exchange of gaseous mercury at the largest active landfill in Asia, *Atmospheric Environment*, 79, 188-197,
736 2013a.

Zhu, W., Sommar, J., Li, Z., Feng, X., Lin, C.-J., and Li, G.: Highly elevated emission of mercury vapor due to
738 the spontaneous combustion of refuse in a landfill, *Atmospheric Environment*, 79, 540-545, 2013b.

Zhu, W., Sommar, J., Lin, C.-J., and Feng, X. B.: Air-surface exchange of Hg⁰ measured by collocated
740 micrometeorological and enclosure methods - part II: bias and uncertainty analysis, *Atmos. Chem. Phys.*, in
review, 2014a.

742 Zhu, W., Sommar, J., Lin, C.-J., Feng, X. B., Shang, L. H., and Zhang, Y. T.: Seasonal elemental mercury gas
exchange over a wheat-corn rotation cropland in the North China Plain, Unpublished data, 2014b.

744

746

748 **Table 1** Summary of observed meteorological variables, Hg⁰ concentrations, vertical Hg⁰ concentration
 gradients and Hg⁰ fluxes for two campaigns

750

Variables	Unit	Bare surface (IC #1, DOY 309-329)			Canopy surface (IC #2, DOY 106-115)		
		Range	Mean	Median	Range	Mean	Median
AGM flux	ng m ⁻² h ⁻¹	-124.8-220.2	5.3	-0.5	-155.0-289.7	10.8	2.8
MBR flux	ng m ⁻² h ⁻¹	-151.1-181.6	7.2	0.1	-148.7-269.1	9.3	1.4
REA flux	ng m ⁻² h ⁻¹	[—]	[—]	[—]	-283.5-611.6	17.3	8.8
NDFC flux	ng m ⁻² h ⁻¹	-21.0-108.9	7.6	-0.9	[—]	[—]	[—]
TDFC flux	ng m ⁻² h ⁻¹	-23.4-43.4	2.2	-1.7	[—]	[—]	[—]
Sensible heat flux	W m ⁻²	-740.8-158.7	11.2	-0.4	-243.9-167.6	12.3	-5.3
Hg ⁰ concentration	ng m ⁻³	1.34-8.17	3.26	3.12	1.20-7.28	3.40	3.50
Normalized vertical Hg ⁰ conc. gradients	ng m ⁻⁴	-0.49-0.33	0.013	0.014	-0.48-0.25	-0.013	-0.01
Friction velocity (u*)	m s ⁻¹	0.008-0.519	0.124	0.082	0.012-1.585	0.272	0.23
Wind speed	m s ⁻¹	0.03-6.25	1.52	1.18	0.11-8.40	2.69	2.42
Global radiation (daytime)	W m ⁻²	1.9-591.9	261.2	241.9	1.9-890.6	299.4	237.5
Air temperature	°C	-3.54-15.14	6.19	6.11	0.84-17.36	8.91	8.25
Soil temperature	°C	-0.23-13.48	5.32	5.03	1.51-21.32	10.02	9.31
Relative humidity	%	27.6-98.7	65.2	73.0	35.1-99.6	69.4	73.7
Soil moisture	m ⁻³ m ⁻³	0.04-0.17	0.11	0.11	0.02-0.22	0.14	0.18

752

754 **Table 2** Pearson correlation analysis of hourly Hg⁰ flux from various field measurement techniques and environmental parameters for two campaigns. Shaded part
 in the right and top denote date from IC #2. Bold font denotes a statistically significant correlation coefficient ($p < 0.05$).

756

Variables	MBR flux	AGM flux	TDFC flux	NDFC flux	GEM	u^*	Soil temp.	Global radiation	Air Humi.	Soil moisture	Wind speed
REA flux	0.15	0.09	[-]	[-]	-0.11	0.12	0.10	0.08	-0.15	-0.16	0.12
MBR flux		0.92	[-]	[-]	0.10	-0.08	0.13	0.08	-0.14	-0.13	-0.11
AGM flux	0.81		[-]	[-]	0.11	-0.10	0.15	0.12	-0.14	-0.16	-0.14
TDFC flux	0.23	0.41		[-]	[-]	[-]	[-]	[-]	[-]	[-]	[-]
NDFC flux	0.27	0.47	0.95		[-]	[-]	[-]	[-]	[-]	[-]	[-]
GEM	0.07	0.03	-0.20	-0.16		-0.41	0.39	0.24	0.32	0.24	-0.45
u^*	0.28	0.37	0.50	0.62	0.10		0.32	0.45	-0.65	-0.36	0.99
Soil temp.	0.15	0.26	0.56	0.54	0.44	0.45		0.43	-0.42	-0.17	0.26
Global radiation	0.38	0.48	0.74	0.89	0.13	0.57	0.44		-0.31	-0.03	0.36
Air humidity	-0.17	-0.35	-0.70	-0.69	0.20	-0.46	-0.46	-0.63		0.49	-0.61
Soil moisture	0.06	0.14	0.46	0.38	0.06	0.19	0.29	0.24	-0.22		-0.33
Wind speed	0.27	0.35	0.50	0.61	0.15	0.95	0.49	0.56	-0.50	0.19	

758

760 **Fig. 1.** Schematic drawing illustrating the collocated MM and DFCs instrumentation set-ups. P, MFC and FM indicate a pressure transmitter, mass flow controller and flow meter of rotameter type respectively.

762 **Fig. 2.** General meteorological parameters and ambient GEM concentration in the two campaigns. Upper panel: relative humidity (blue open circles), canopy leaf wetness (light blue line filled down), air
764 temperature (red filled diamonds) and rainfall (black bar), middle panel: wind speed (green line) and wind direction (dark green open circles filled down) , and lower panel: ambient GEM concentration (dark purple
766 open circles), global radiation (orange squares filled down) and σ_w/u_* (magenta line)

768 **Fig. 3.** Polar histograms of 20-min averaged wind speed (m s^{-1}) and Hg^0 concentration (ng m^{-3}): (A) Wind
rose during IC #1; (B) Hg^0 concentration rose during IC #1; (C) wind rose during IC #2; (D) Hg^0
770 concentration rose during IC #2

772 **Fig. 4.** Time series of GEM gradients, GEM fluxes measured in: (A) IC #1 using MM and DFCs
techniques; (B) IC #2 using MM techniques. The color code (green-yellow-red) denotes the quality
774 (high-moderate-low) of turbulent flux data derived from general tests and black bars given in
corresponding plots represent absolute flux uncertainties.

776

Fig. 5. Distributions of Hg^0 flux derived from DFC measurements (Upper panel: TDFC, Lower panel: NDFC).
778 The tripartite panels consists from left to right of a shadowgram (a suite of overlaid histograms with different
bin widths), a Box & Whiskers plot (the ends of the box represent Q1 and Q3 and the whiskers denote ± 1.5
780 times the interquartile range, $\text{IQR} = \text{Q3} - \text{Q1}$. Sample points further away are given as individual markers) and
the corresponding normal quantile plot (the unbroken solid line signifies the expected normal cumulative
782 distribution and the dashed intervals the Lilliefors confidence bounds. The scale of the upper and lower abscissa
indicates normal quantile and probability). Furthermore, in the Box & Whiskers plot, mean is indicated by a
784 filled diamond while the median is the line within the box. The bracket outside of the box identifies the shortest
half, which is the most dense 50% of the observations.

786

Fig. 6. Scatter plot of Hg^0 flux obtained from TDFC and NDFC measurement (green open circles), and the
788 NDFC calculated using Eq.1 versus TDFC flux (grey filled squares).

790 **Fig. 7.** Overview of the distributions of turbulent Hg^0 flux measured by the MM techniques (panel A: IC #1,
panel B: IC #2). See Fig. 5 for a detailed description of the composite plots.

792

Fig. 8. Scatter plots of 20-min MBR versus AGM flux during IC#1 (upper panel) and IC#2 (lower panel). The
794 plots on the right hand side depicting specific data for which $|H| < 20 \text{ W m}^{-2}$.

796 **Fig. 9.** Diurnal variation of Hg^0 flux measured with various techniques represented as Box & whiskers

plots. . The two box horizontal border lines represent 25th, and 75th percentiles from bottom to top, and
798 whiskers indicate the 10th and 90th percentiles. Bold line and fine line in the box indicate mean and
median flux.

800

Fig. 10. Smoothed diurnal cycles of Hg^0 flux and Hg^0 concentration derived from hourly averaged input
802 data.

804 **Fig. 11.** Time series cumulative Hg^0 flux using various techniques for: (A) IC #1 over bare soil; (B) IC #2
over wheat canopy.

806

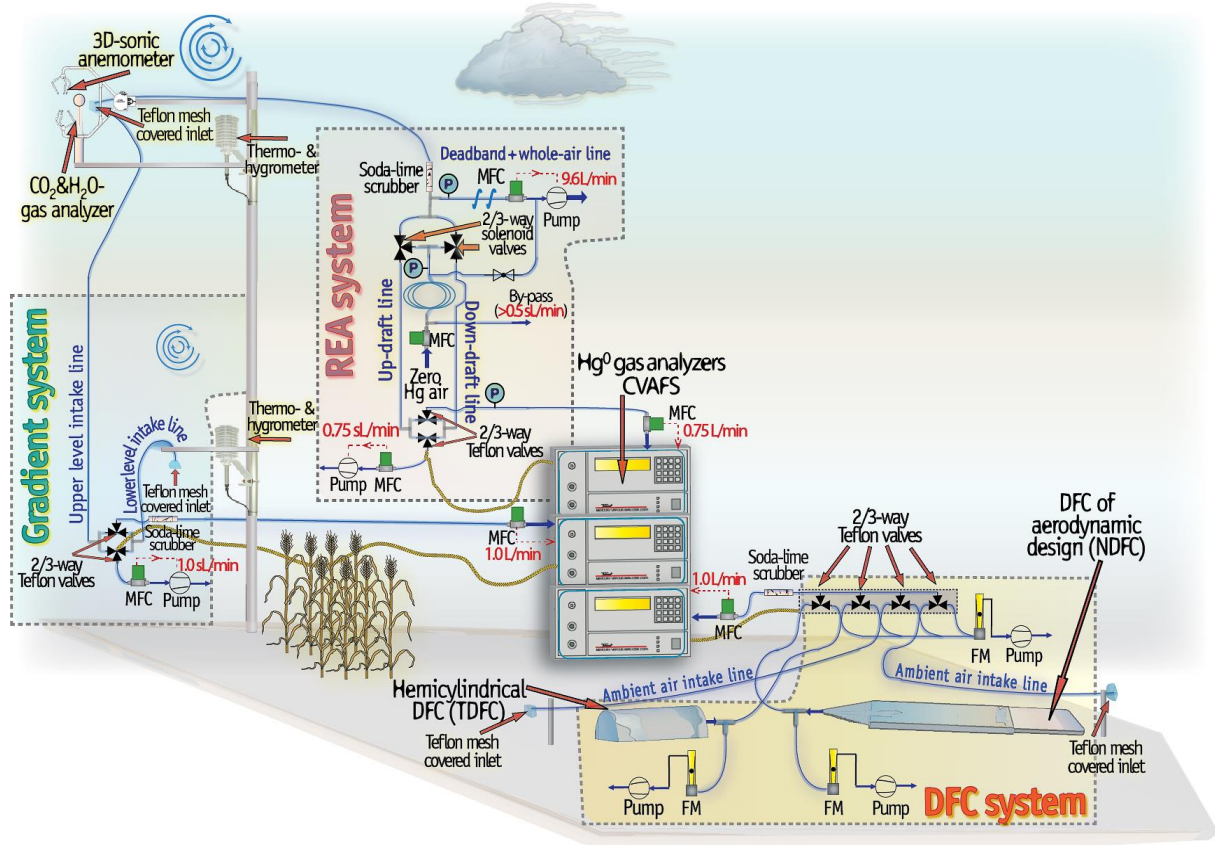
Fig. 12. Scatter plots of: (A) MBR vs. NDFC/TDFC Hg^0 flux; (B) time-series cumulative flux difference
808 between the MBR- and NDFC/TDFC method.

810

812

Fig. 1. Schematic drawing illustrating the collocated MM and DFCs instrumentation set-ups. P, MFC and FM indicate a pressure transmitter, mass flow controller and flow meter of rotameter type respectively.

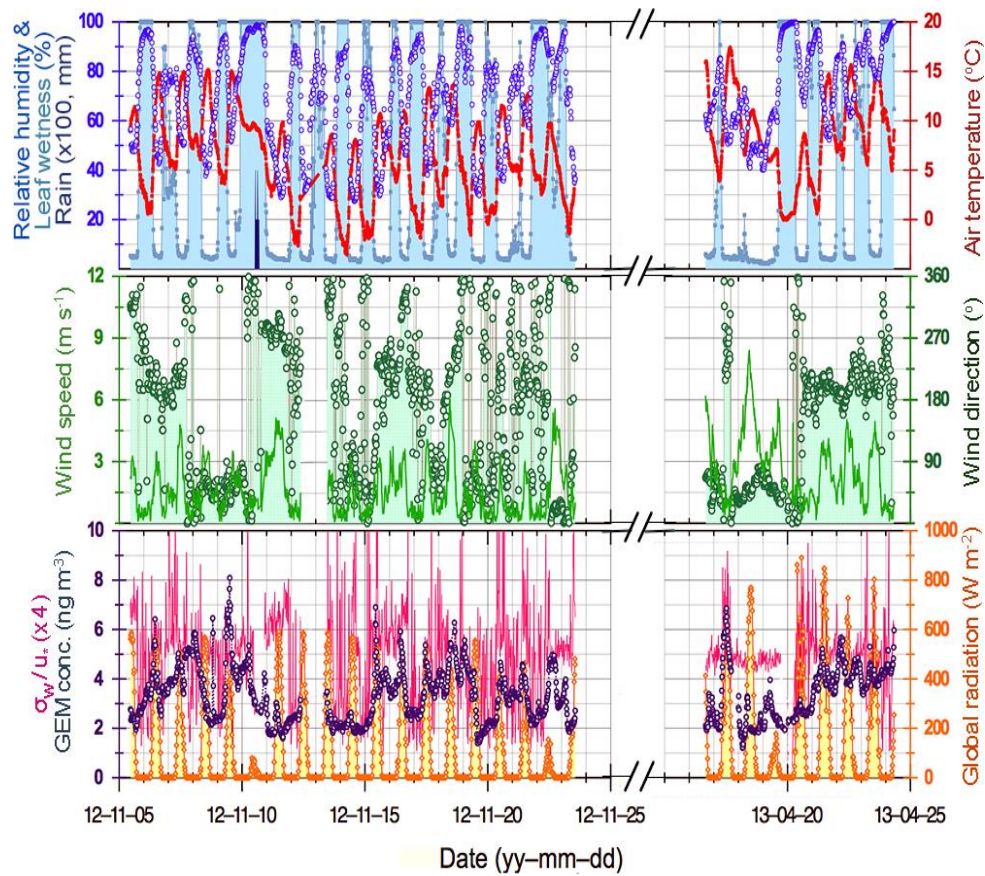
814



816

818

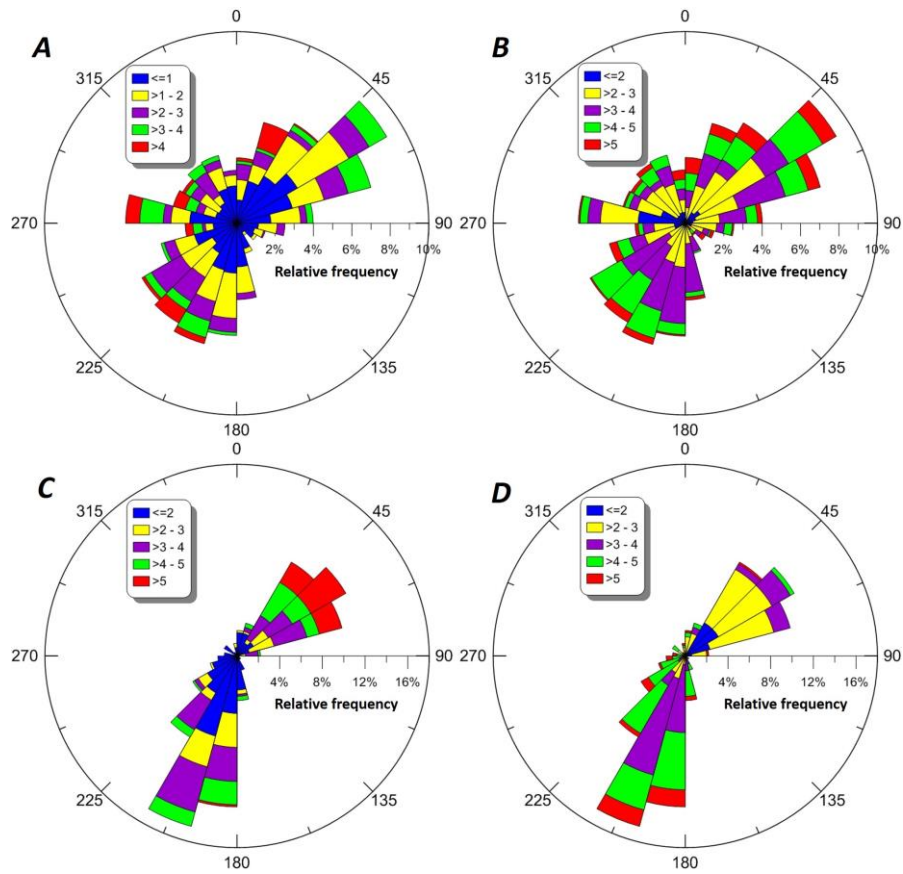
820 **Fig. 2.** General meteorological parameters and ambient GEM concentration in the two campaigns. Upper
 822 panel: relative humidity (blue open circles), canopy leaf wetness (light blue line filled down), air
 temperature (red filled diamonds) and rainfall (black bar), middle panel: wind speed (green line) and wind
 direction (dark green open circles filled down) , and lower panel: ambient GEM concentration (dark purple
 824 open circles), global radiation (orange squares filled down) and σ_w/u_* (magenta line)



826

828

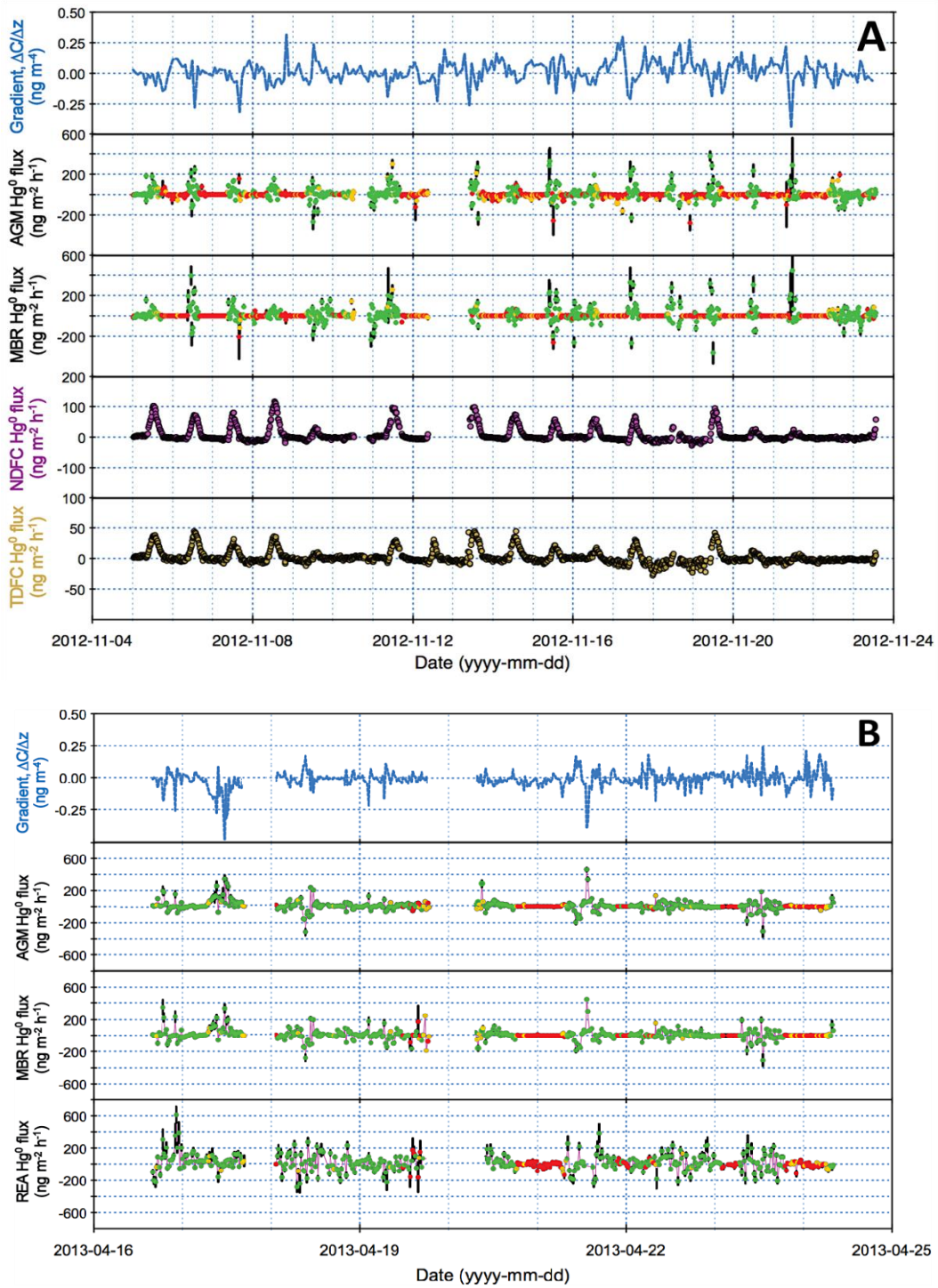
830 **Fig. 3.** Polar histograms of 20-min averaged wind speed (m s^{-1}) and Hg^0 concentration (ng m^{-3}): (A) Wind
831 rose during IC #1; (B) Hg^0 concentration rose during IC #1; (C) wind rose during IC #2; (D) Hg^0
832 concentration rose during IC #2



834

836

838 **Fig. 4.** Time series of GEM gradients, GEM fluxes measured in: (A) IC #1 using MM and DFCs
 840 techniques; (B) IC #2 using MM techniques. The color code (green-yellow-red) denotes the quality
 842 (high-moderate-low) of turbulent flux data derived from general tests and black bars given in
 corresponding plots represent absolute flux uncertainties.



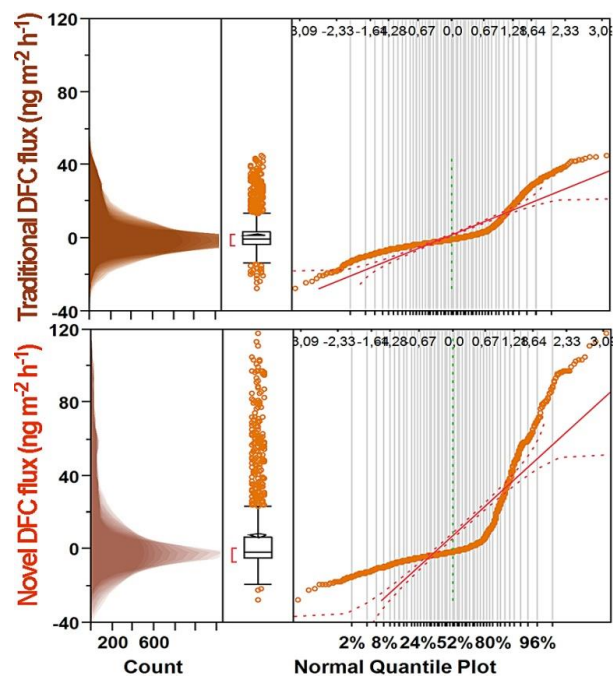
844

846

Fig. 5. Distributions of Hg^0 flux derived from DFC measurements (Upper panel: TDFC, Lower panel: NDFC).

848 The tripartite panels consists from left to right of a shadowgram (a suite of overlaid histograms with different
850 bin widths), a Box & Whiskers plot (the ends of the box represent Q1 and Q3 and the whiskers denote ± 1.5
852 times the interquartile range, $IQR = Q3 - Q1$. Sample points further away are given as individual markers) and
854 the corresponding normal quantile plot (the unbroken solid line signifies the expected normal cumulative
distribution and the dashed intervals the Lilliefors confidence bounds. The scale of the upper and lower abscissa
indicates normal quantile and probability). Furthermore, in the Box & Whiskers plot, mean is indicated by a
filled diamond while the median is the line within the box. The bracket outside of the box identifies the shortest
half, which is the most dense 50% of the observations.

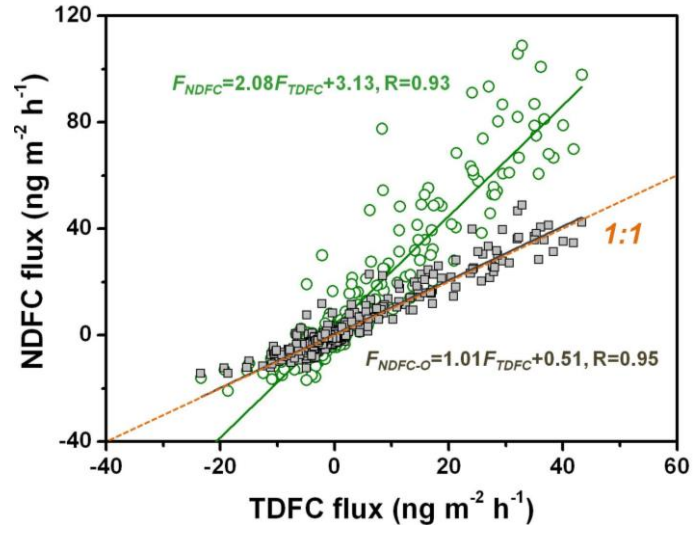
856



858

860

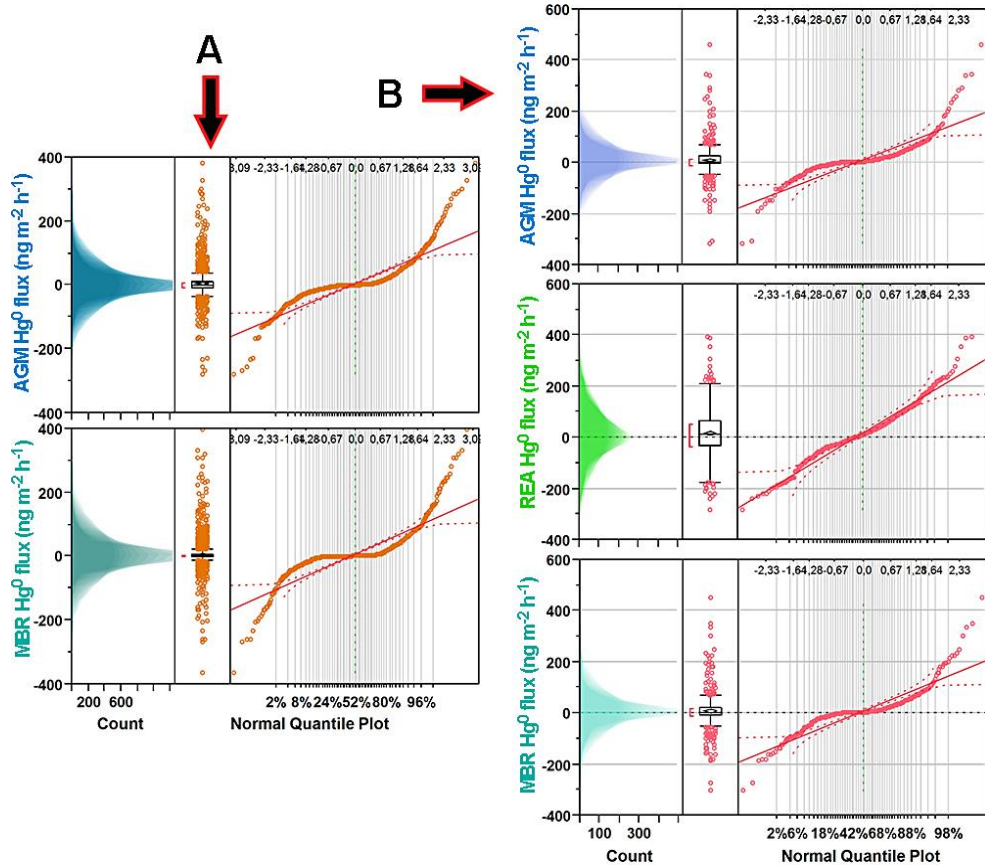
Fig. 6. Scatter plot of Hg^0 flux obtained from TDFC and NDFC measurement (green open circles), and the
862 NDFC calculated using Eq.1 versus TDFC flux (grey filled squares).



864

866

868 **Fig. 7.** Overview of the distributions of turbulent Hg^0 flux measured by the MM techniques (panel A: IC #1,
 870 panel B: IC #2). See Fig. 5 for a detailed description of the composite plots.

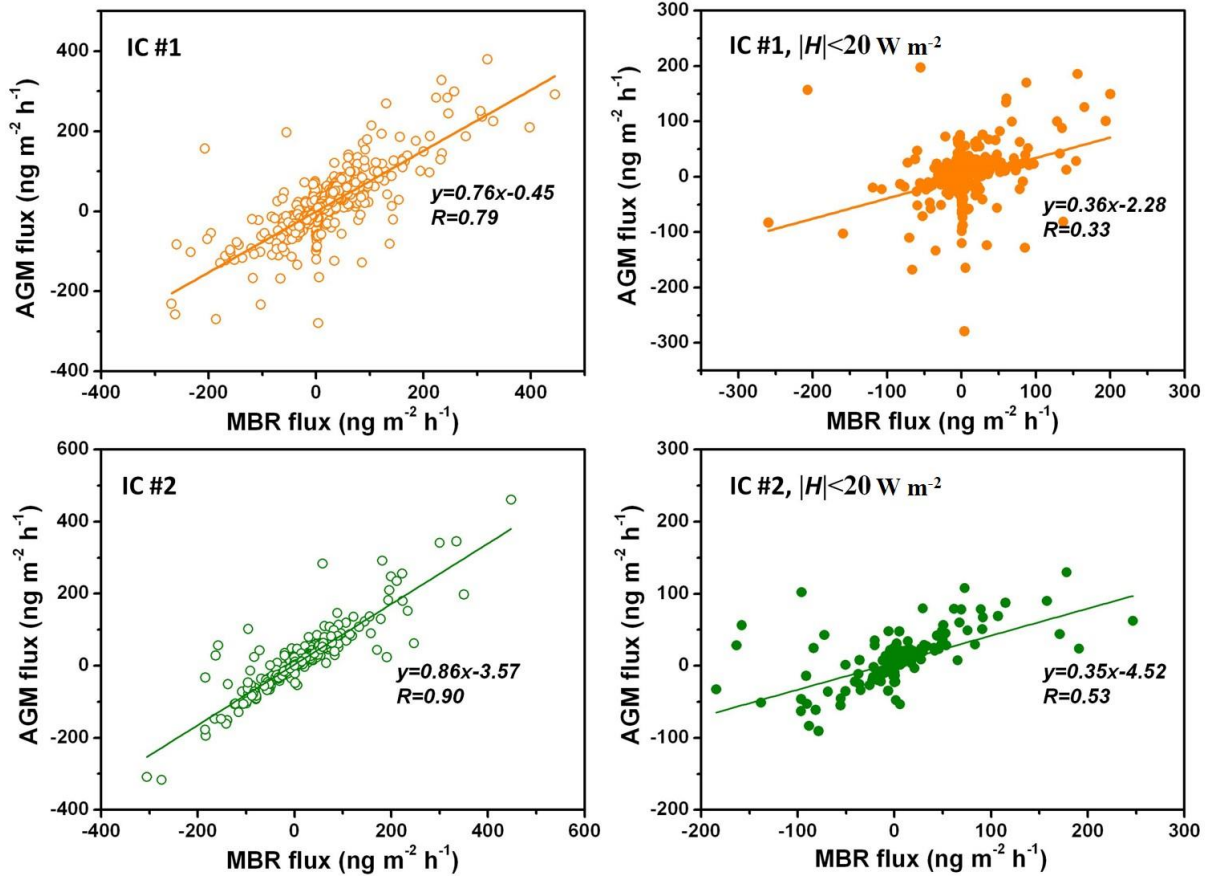


872

874

Fig. 8. Scatter plots of 20-min MBR versus AGM flux during IC#1 (upper panel) and IC#2 (lower panel). The

876 plots on the right hand side depicting specific data for which $|H| < 20 \text{ W m}^{-2}$.

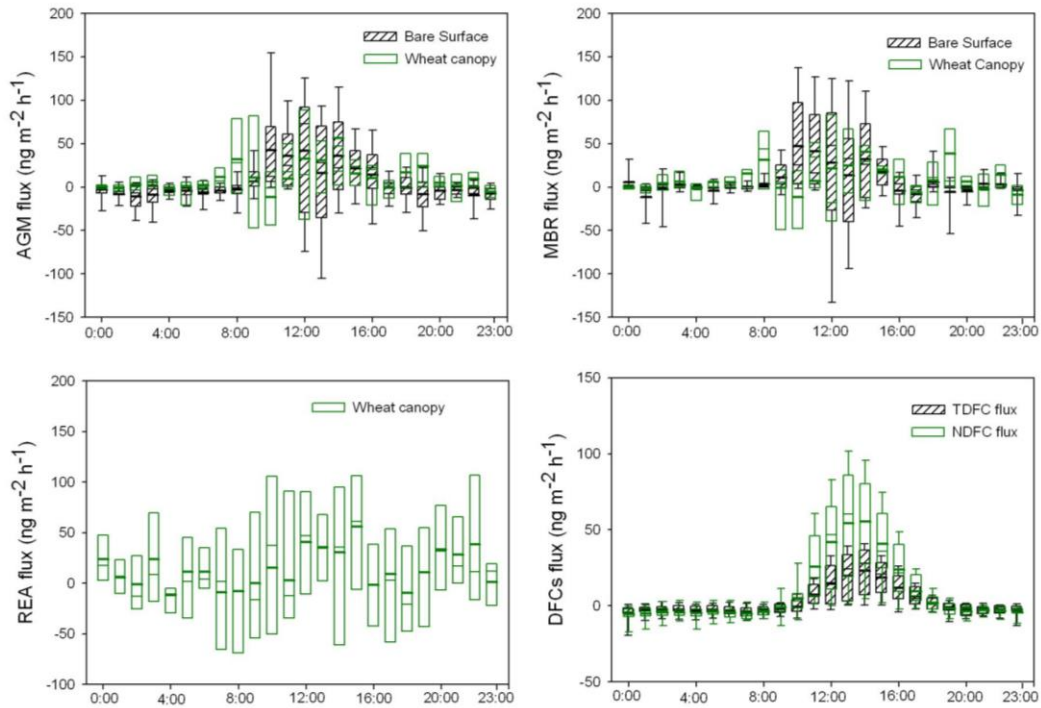


878

880

882 **Fig. 9.** Diurnal variation of Hg^0 flux measured with various techniques represented as Box & whiskers
plots. . The two box horizontal border lines represent 25th, and 75th percentiles from bottom to top, and
884 whiskers indicate the 10th and 90th percentiles. Bold line and fine line in the box indicate mean and
median flux.

886

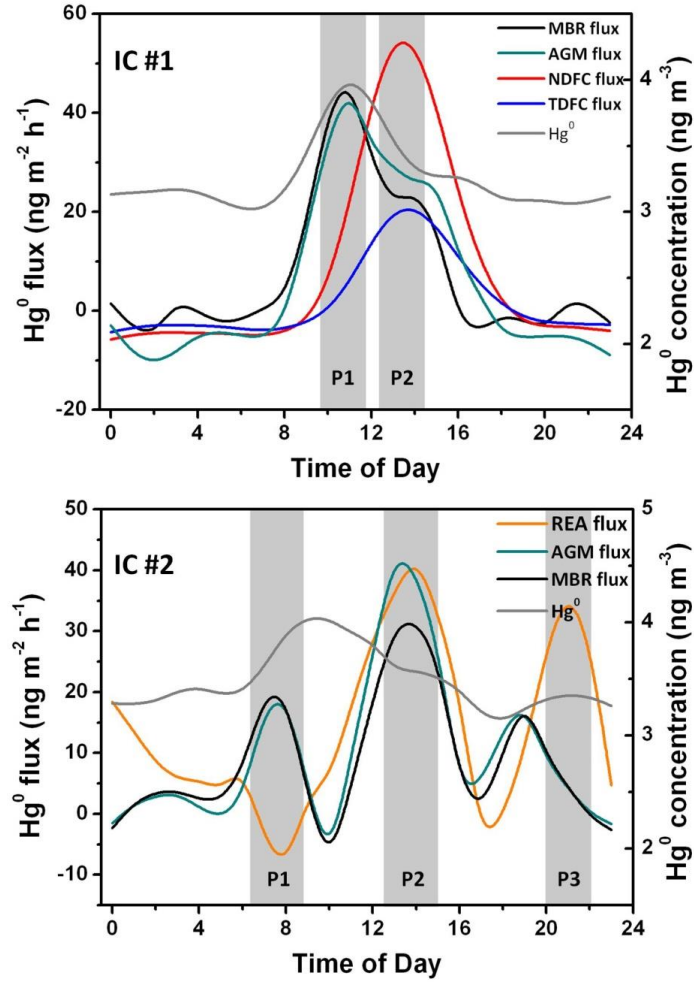


888

890

Fig. 10. Smoothed diurnal cycles of Hg^0 flux and Hg^0 concentration derived from hourly averaged input data.

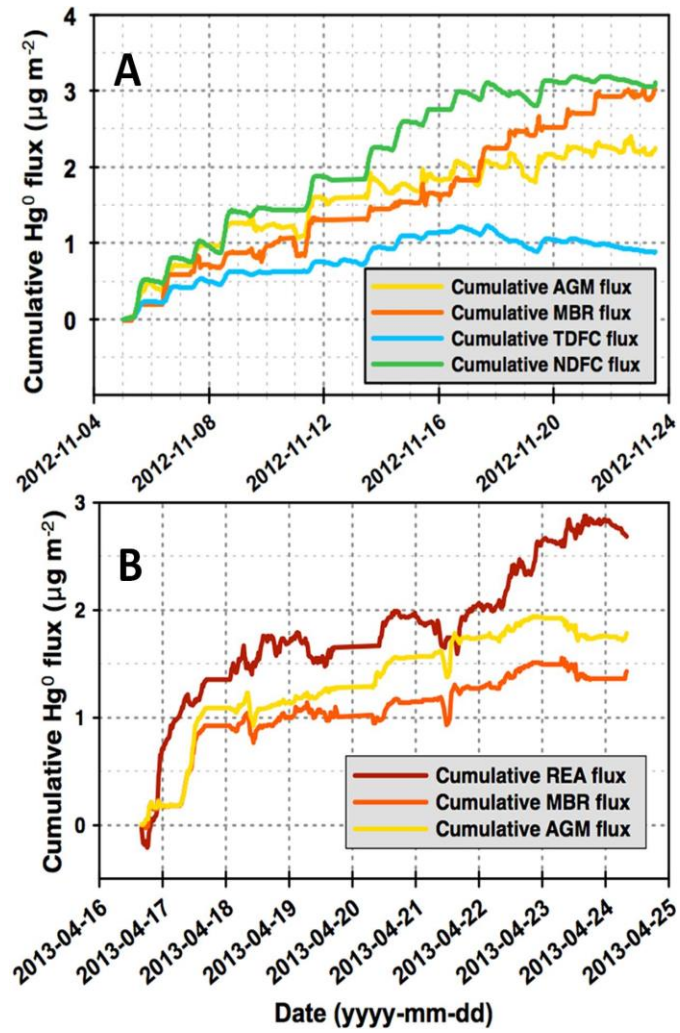
892



894

896

898 **Fig. 11.** Time series cumulative Hg^0 flux using various techniques for: (A) IC #1 over bare soil; (B) IC #2
900 over wheat canopy.

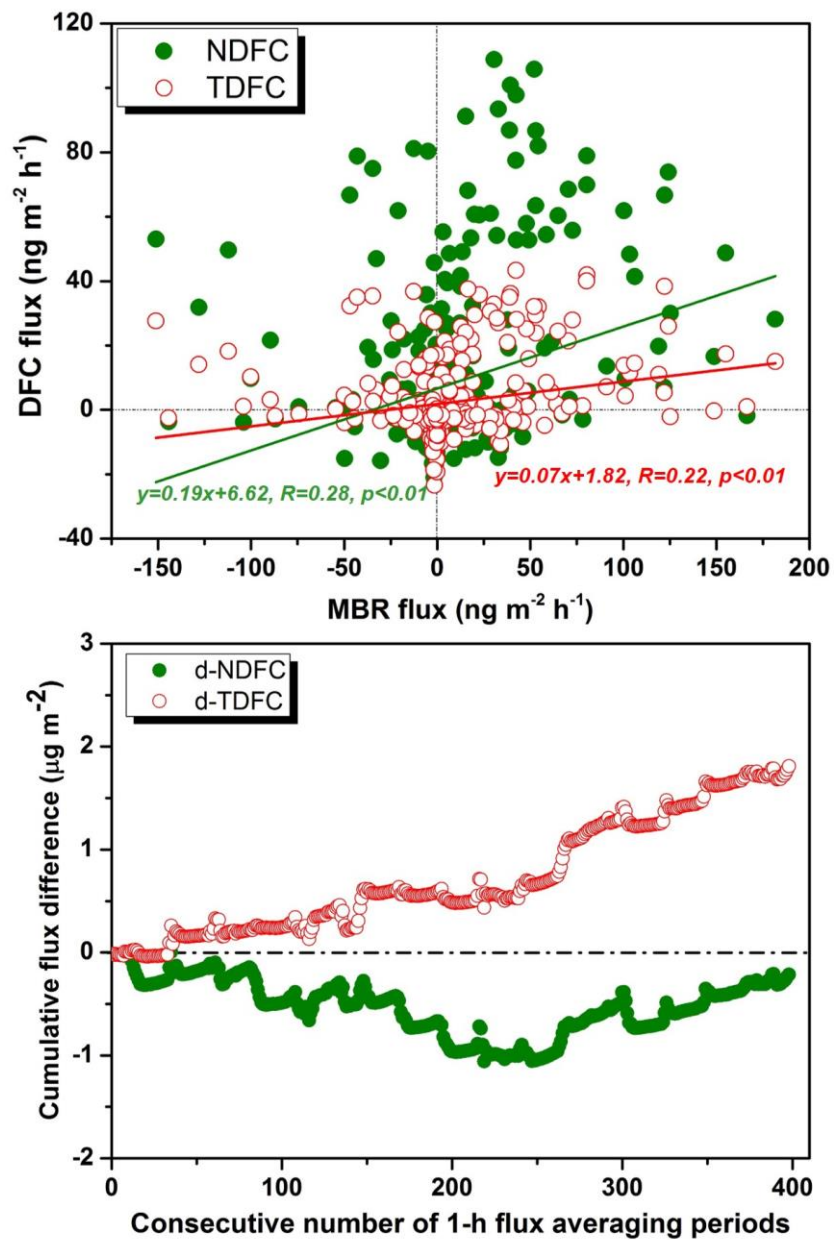


902

904

Fig. 12. Scatter plots of: (A) MBR vs. NDFC/TDFC Hg^0 flux; (B) time-series cumulative flux difference between the MBR- and NDFC/TDFC method

906



908

910